ALMA MATER STUDIORUM
UNIVERSITA' DI BOLOGNA

SECONDA FACOLTA' DI INGEGNERIA
CON SEDE A CESENA

CORSO DI LAUREA
IN INGEGNERIA AEROSPAZIALE
Sede di Forlì

TESI DI LAUREA
in Aerodinamica applicata LM

Hot wire manufacturing and resolution effects in high Reynolds number flows

STUDENTE :
Tommaso Fiorini

RELATORE:
Alessandro Talamelli

Anno accademico 2011/2012
III Sessione

Contents

Chapter 1

Introduction

1.1 Turbulence

The majority of flows that we encounter in nature or in practical applications are of turbulent nature. Turbulence appears as a random and evolving phenomenon, an unstable and irregular system of different scale eddies, in contrast to the laminar flow regime. At first glance the process appears chaotic, so much that infact a reliable prediction on its behaviour may seem impossible. Despite this, the equations governing turbulence have been known for a long time and would in principle allow for a direct and deterministic approach on the subject. It is however for their intrinsic complexity that we are forced to take a statistical approach when we study turbulence. And indeed turbulence remains one of the biggest unresolved issues of modern physics. The interest in turbulence is not only limited to the field of base research, motivated by the desire to gain a deeper physical understanding of the nature of such a rich and complex phenomenon. As already said, turbulence is present in an vast number of engineering applications: fluid operating machinery, aeronautics and naval applications, meteorology and automotive vehicles. In figure 1.1 are shown some examples of these applications. Osborne Reynolds was the first to carry out a systematic study on the onset of turbulence and the parameters governing the transition. In his universally famous pipe flow experiment of 1883, he realised that the transition to turbulence depends on a dimensionless parameter, that since then has been known as the *Reynolds number*

$$Re = \frac{UL}{\nu} \tag{1.1}$$

Figure 1.1: Turbulence in engineering applications.

Where U and L are the flow's characteristic length and velocity scales, and ν is the kinematic viscosity. Obviously the length and velocity scales used in the Reynolds number definition depend on the particular flow considered. Reynolds found out that transition to turbulence started when this dimensionless parameter reached a certain value, which is generally referred to as the *critical Reynolds number*. But not only is the Reynolds number the foundamental parameter for stability, it can also be used to determine dynamic similitude between different experimental cases. High Reynolds numbers cases are of extreme importance to draw conclusions regarding the general nature of turbulence flow physics, but also because the practical engineering situations in aeronautics, vehicle applications, meteorology and energy conversion processes, take place at high Reynolds number. High Reynolds number turbulence is carachterised by the presence of a wide range of different scales, from the big eddies whose dimensions are associated with the flow geometry to the smallest eddies. To use the famous words from Richardson (1920):

> *"Big whorls have little whorls*
> *That feed on their velocity,*
> *And little whorls have lesser whorls*
> *And so on to viscosity."*

Larger eddies is where the turbulent kinetic energy is introduced in the flow, they are dependent on the particular flow geometry and are dominated by inertial forces. From the large eddies energy is transferred to the smaller ones in a process that is known as *energy cascade*; this happens until eddies reach their minimum dimension and dissipation of the turbulent kinetic energy into heat is caused by viscous forces. These small structures are called *Kolmogorov scale*, from the name of the mathematician that first quantified them in 1941. Unlike large scale eddies they are believed to be independent on the flow geometry and have universal and isotropic properties. The variety of turbulent scales and their difference in dimensions grows with increasing Reynolds number. In other words the higher the Reynolds number, the smaller the dissipation (Kolmogorov) scale becomes compared to the big scales. In recent years the exponential increase in computing power has allowed us to use direct numerical simulations (DNS) in the study of turbulence for higher Reynolds number. In fully resolved DNS the Navier-Stokes equations governing turbulence are numerically resolved up to their finest spatial and temporal scales, without the use of any model. Despite these recent advances, the numerical approach remains limited in Reynolds number, thus it cannot be used for cases of greatest practical interest. Another problem is the fact that the computational time required to obtain statistical convergence, especially for high-order statistics, may become prohibitive. Because of this, experimental study often remains the only option for answering questions in high reynolds number turbulent flows. In particular hot-wire anemometry has become since its introduction the preferred technique for turbulent velocity measuraments, thanks to its excellent temporal and spatial resolution. Unfourtunately, despite the very small physical dimension of the sensor element, for high Reynolds number flows spatial resolution errors can be introduced in the measurement. This happens when the smaller turbulent scales are smaller than the sensor element. And it happens most of the time when investigating particular flows, like wall turbulence. Hot-wire sensors have the great advantage of being relatively simple and can be manufactured using cheap materials and techniques, the only difficulty involved being their extremely small dimension. The aim of this thesis is to set up the procedure and equipment needed for hot-wire construction, then to manufacture sensors suited for high Reynolds measurements with characteristics in terms of spatial and temporal resolution exceeding the available commercial sensors. And finally to test their response in turbulent high Reynolds number flow.

Chapter 2

Theoretical background

2.1 Turbulent scales and energy cascade

As already said in the introduction, one of the peculiarity of turbulent flows is the existence of a wide range of different scale eddies. The most obvious big scales are the ones associated to the macroscopic geometric features of the flow: for a boundary layer flow is the boundary layer thickness δ, for a channel flow is its half-height $h/2$ and for a pipe or round jet flow is the radius R. The idea of an energy cascade was put forward by Richardson (1922); essentially it states that kinetic energy "enters" turbulence at big scales via a production mechanism, then it is transferred in a inviscid way to scales gradually smaller until is dissipated at small scales by viscous action. It appears evident that the dissipation rate ϵ at small scales must then be equal to the rate at wich energy is produced at large scales. According to Richardson, eddies can be characterised by a length l, a velocity $u(l)$ and a time scale $\tau(l) = l/u(l)$. The big eddies have a length l_0 comparable with L, a characteristic velocity u_0 that is of the order of the root mean square of the turbulence intensity that is comparable with U, hence the big eddies' Reynolds number $l_0 u_0(l)/\nu$ is large and viscous effect are negligible. Later Kolmogorov in his 1941 work identified this small scales (the ones that are now known with his name). He observed that as l decreased, $u(l)$ and $\tau(l)$ decreased as well. He formulated a theory that can be summarized in three hypothesis:

- At sufficiently high Reynolds number, small-scale ($l << l_0$) turbulence is statistically isotropic.

This hypothesis is also known as *local isotropy*. In other words, while large eddies are anisotropic (their statistics depend on the direction considered), for

small scales, turbulent flows "forget" the information given by the mean flow field and the flow's boundary conditions. Furthermore, these statistics become universal:

- At sufficiently high Reynolds number, statistics at small scale have an universal form determined by ν and ϵ.

That is because at small scales dissipation of the energy transferred from bigger scales takes place via viscous process. The rate at which the energy is dissipated is ϵ, while ν is the cinematic viscosity. On these two parameters the length, velocity and timescale of the Kolmogorov scale η can be defined

$$\eta \equiv (\nu^3/\epsilon)^{1/4} \tag{2.1}$$

$$u_\eta \equiv (\epsilon\nu)^{1/4} \tag{2.2}$$

$$\tau_\eta \equiv (\nu/\epsilon)^{1/2} \tag{2.3}$$

Kolmogorov also derived the ratio between the large eddie size and the dissipative eddie size (based on the scaling $\epsilon \approx u_0^3/l_0$):

$$l_0/\eta \approx Re^{3/4} \tag{2.4}$$

which means that with increasing Reynolds number, the range of scales between l_0 and η increases as well. Ultimately, at very high reynolds number there must be a range of scales of length l that are very small compared to l_0 but still very big when compared with the Kolmogorov scale.

- At sufficiently high Reynolds number, statistics for scales l, with $\eta << l << l_0$, have a universal form determined solely by ϵ and indipendent on ν.

this range of scales is called *inertial subrange* and it is only marginally affected by viscosity, it depends almost esclusively on the energy transfer rate $\mathcal{T}_e \approx \epsilon$. Hence its statistics are defined only by the dissipation rate. In figure 2.1 is shown a schematic of different scales and their interactions.

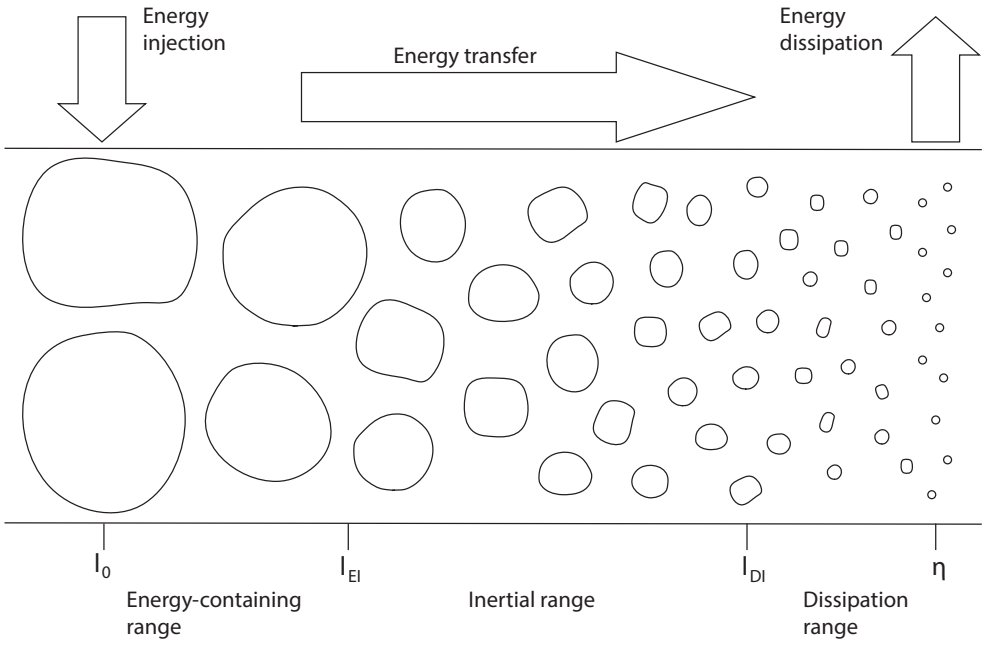

Figure 2.1: Energy cascade schematics

2.2 Statistical tools for turbulence

As already mentioned, in order to study turbulence, a statistical approach is taken, as the complexity of the phenomenon makes it easier to characterize it as a purely random process. In this section a brief explanation of the statistical notions used later in the thesis will be provided.

2.2.1 The probability density function

The *probability density function*, or PDF, of a random variable $u(t)$ is a function that describes the relative likelihood for this random variable to assume a certain value. If the PDF of random variable is known, then all the statistical moments of any order are known. We first introduce the *cumulative distribution function* of a random variable $u(t)$, $F_u(U)$. It is defined as the probability that $u(t)$ has to take on a value that is smaller or equal to U:

$$F_u(U) = P(u(t) \leq U) \tag{2.5}$$

Every cumulative distribution function is a monotone non-decreasing function. Furthermore, whatever the random variable, $F_u(-\infty) = 0$ and $F_u(+\infty) = 1$. The probability that the random variable assumes a value that is between two

values U_1 and U_2, with $U_1 \leq U_2$ can be expressed with cumulative distribution functions:

$$P(U_1 \leq u(t) \leq U_2) = F_u(U_2) - F_u(U_1) \tag{2.6}$$

The probability density function $f(U)$ is then defined as:

$$f(U) \equiv \lim_{\Delta U \to 0} \left(\frac{F_u(U + \Delta U) - F_u(U)}{\Delta U} \right) \tag{2.7}$$

or, in other words:

$$f(U) = \frac{dF_u(U)}{dU} \tag{2.8}$$

and has the following properties:

$$f(U) \geq 0, \tag{2.9}$$

$$\int_{-\infty}^{+\infty} f(U)dU = 1, \tag{2.10}$$

$$F_u(U) = \int_{-\infty}^{U} f(\chi)d\chi \tag{2.11}$$

2.2.2 Statistical moments

The *mean* is the first order statistical moment:

$$<u>= \int_{-\infty}^{+\infty} uf(u)du \tag{2.12}$$

from the mean, the *fluctuations* can be defined:

$$u' \equiv u - <u> \tag{2.13}$$

Since the mean value of fluctuations is always null, to further describe the statistics of the process, higher order moments are introduced. The second order moment is the *variance*, that gives an idea of the fluctuations' magnitude.

$$<u'^2>= \int_{-\infty}^{+\infty} u'^2 f(u)du \tag{2.14}$$

The square root of the variance is known as the *standard deviation* or *root mean square*:

$$\sigma_u = \sqrt{<u'^2>} \tag{2.15}$$

likewise, other statistical moments can be introduced; the nth centered statistical moment of the random variable $u(t)$ is defined as:

$$<u'^n>=\int_{-\infty}^{+\infty} u'^n f(u)du \tag{2.16}$$

of particular interest to turbulence study, are the third and fourth order moments, the *skewness* and *flatness*. They are usually normalized with the root mean square of appropriate order, giving the skewness and flatness factors:

$$S_u = \frac{<u'^3>}{\sigma_u^3} \tag{2.17}$$

$$F_u = \frac{<u'^4>}{\sigma_u^4} \tag{2.18}$$

The skewness and flatness factors are used to describe particular properties of

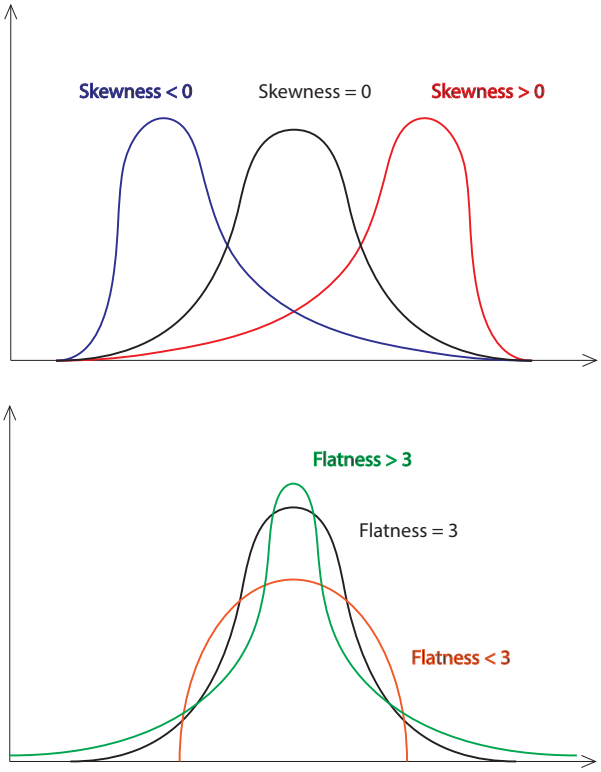

Figure 2.2: Top: examples of different skewness PDFs. Bottom: examples of different flatness PDFs

the probability density function. The skewness is a measure of the symmetry of

the PDF, and is equal to zero when the distribution is symmetrical (see figure 2.2). The flatness on the other hand indicates the relative flatness or peakedness of the distribution function, for a gaussian PDF its value is 3.

2.2.3 Velocity averaging in turbulent flows

In turbulence study, the istantaneous velocity components, U_i are divided into their mean and fluctuating part, in what is known as *Reynolds decomposition*.

$$U_i = <U_i> + u'_i \tag{2.19}$$

where U_i is one istantaneous velocity component, $<U_i>$ is its mean part and u'_i is its fluctuating part. The correct way to obtain the mean would be with an *ensemble average*. Let's suppose we can conduct the experiment n times, each time measuring the velocity in the point $\vec{x}$ at the time t. Then the velocity ensemble average in the point $\vec{x}$ and at the time t is given by:

$$<U_i> (\vec{x}, t) \equiv \frac{\sum_{j=1}^{n} U_{i,j}(\vec{x}, t)}{n} \tag{2.20}$$

Where $U_{i,j}(\vec{x}, t)$ denotes the ith component of velocity measured in the jth experiment, at time t and in the position $\vec{x}$. However, this is not how averages are taken in experimental fluid dynamics, because most of the turbulent flows studied are *statistically stationary*. This means that their statistical properties are not dependent on the time t, and have the same behaviour averaged over time as averaged over different experiments. So the mean part of velocity, for a turbulent but statistically stationary flow is defined as a temporal mean $\overline{U_i}$:

$$<U_i> (\vec{x}, t) = \overline{U_i(\vec{x}, t)} \equiv \frac{1}{T} \int_0^T U_i(\vec{x}, t) dt \tag{2.21}$$

When a process satisfies this relationship is said to be *ergodic*. All the mean values that will be used when carring out the experimental part, will be taken averaging over time.

2.2.4 Correlation

When the random variable is a function of time, the phenomenon is called *random process* and will be indicated as $u(t)$. Even if the PDF is known in a certain place in the flow field, this does not give any joint informations about two different points in the flow; indeed very different statistical processes might

have the same PDF. For this purpose multi-time and multi-space statistical properties are used. The *auto-covariance* is defined as:

$$R(\tau) \equiv <u'(t)u'(t+\tau)> \tag{2.22}$$

If the process is statistically stationary, the auto covariance does not depend on t but only on τ. Auto-covariance gives an idea of the time that it takes the turbulent flow to "forget" its past history at a particular point. From the auto-covariance the *correlation function* can be defined:

$$\rho(\tau) \equiv \frac{<u'(t)u'(t+\tau)>}{<u'(t)^2>} \tag{2.23}$$

it has the following properties:

$$\rho(0) = 1, \tag{2.24}$$

$$|\rho(\tau)| \leq 1 \tag{2.25}$$

In figure 2.3 is shown the streamwise autocorrelation function $\rho_{uu}(\tau)$ plotted against the lag time τ. As can be seen, the correlation diminishes rapidly as

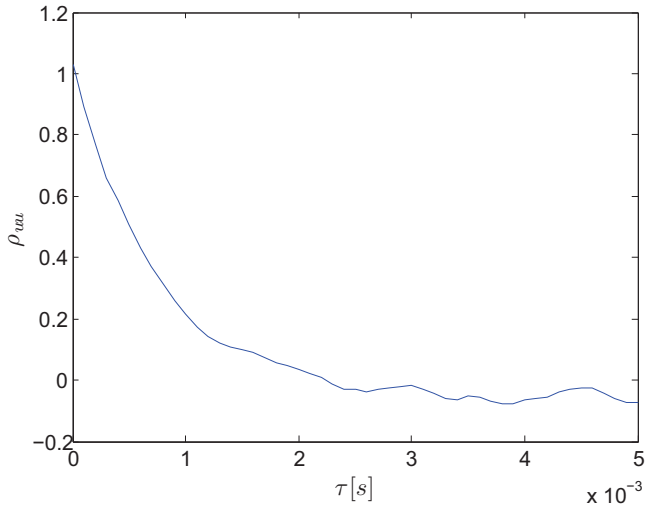

Figure 2.3: Example of streamwise autocorrelation function obtained from current velocity measurements, as a function of the lag time τ.

τ increases. When its value reach zero it means that the fluctuations at time $t+\tau$ are no longer correlated to the ones at time t. A time scale called *integral*

time scale can be defined:

$$\Lambda_t \equiv \int_0^\infty \rho(\tau) d\tau \tag{2.26}$$

The same considerations on fluctuation correlation can be made using space instead of time as the parameter. Covariance can be defined using fluctuations from different points in space but at the same time, instead of the same point but different times. If this is the case the *covariance* becomes a multi-space and single-time statistical property:

$$R_u(\vec{r}) \equiv <u'(\vec{x},t)u'(\vec{x}+\vec{r},t)> \tag{2.27}$$

from this, in the same manner as before, the *spatial correlation function* is defined:

$$\rho_u \equiv \frac{<u'(\vec{x},t)u'(\vec{x}+\vec{r},t)>}{<u'(\vec{x},t)^2>} \tag{2.28}$$

$\vec{r}$ is the distance vector between the point $\vec{x}$ and the other point where fluctuations are taken. If the process is statistically stationary, both the covariance and the spatial correlation function are independent on the time t. Spatial correlation functions can be calculated in a moltitude of different ways, for example considering the spatial correlation of a velocity component u_i with itself (which is called *spatial autocorrelation*) or two different velocity components. The autocorrelation can be *longitudinal* if $\vec{r}$ is parallel to ${u'}_i$ or *transverse* if it is perpendicular. Just like the temporal correlation an integral scale can be defined. The *integral length scale* is:

$$\Lambda_l \equiv \int_0^\infty \rho_u(r) dr \tag{2.29}$$

As can be seen in 2.29, integration should be applied over an infinite domain. That's obviously not possible, both in the experimental and in the numerical field. To overcome this problem the spatial correlation function is usually integrated up to its first zero value or, if there is one, to its minimum negative value.

2.2.5 Taylor's hypotesis

Although spatial and temporal correlations of a variable are both theoretically and experimentally two distinct things (the first can be carried out with single point measurements, while the second requires multiple points), It can be asked if there is a connection between the two, or if when we obtain one of this correlations, we can infer anything on the other. In most circumstances, it is much

simpler to perform measurements at a single point and different times rather than simultaneously at several points. Taylor proposed a simple hypothesis in 1938 where time and space behaviors (along the mean direction of motion) of a fluid-mechanics variable k are simply related by the convection velocity U_c on the mean velocity direction x_1.

$$\frac{\partial k}{\partial t} \approx -U_c \frac{\partial k}{\partial x_1} \tag{2.30}$$

in other words, the diffusion of the quantity k and its transport in directions orthogonal to the mean flow are ignored. This seems like a very coarse approximation but experimental studies have confirmed that i works fairly well in most conditions, one crucial parameter is the value of the convection velocity U_c. The hypothesis is also known as *frozen turbulence* because, in Taylor's original formulation $U_c = \overline{U}$ for every scales, meaning that the flow structures are supposed "frozen" and only convected by the mean local velocity field. When measuring spectral functions, Taylor's hypothesis allows the replacement of the frequency along the mean flow direction with the wavenumber. Experimental work has demonstrated that this semplified approach is not effective and in order to apply the hypothesis with a good degree of approximation, convection velocities different than the mean velocity have to be used; Romano (1995) and Del Alamo & Jimnez (2009) proved it in wall turbulence, where for a correct estimate a lower velocity than the local mean has to be used, depending on the wall distance. It is generally believed that while large scales are convected by the mean flow velocity, small scales are covected with a much lower velocity which depends on the Reynolds number and the particular flow considered.

2.2.6 Power spectral density

As already said, not all informations about a random process can be deduced from its PDF. We've already defined the correlation that gives additional information about the relation between different times or different points in the flow field; now we are going to talk about *power spectral density*. By giving a frequency description of turbulence, it is possible to see what are the most energy-containing frequencies. In order to do so, we use the *Fourier transform*. The Fourier transform converts a mathematical function of time, $f(t)$ into a new function, denoted by $\mathcal{F}(\omega)$ whose argument is angular frequency ($\omega = 2\pi f$). $f(t)$ and $\mathcal{F}(\omega)$ are also respectively known as time domain and

frequency domain representations of the same "event".

$$\mathcal{F}(\omega) \equiv \frac{1}{2\pi} \int_{-\infty}^{+\infty} e^{-i\omega t} f(t) dt \tag{2.31}$$

For continued signals, the kind we deal with in experimental turbulent measures, it makes more sense to define a power spectral density (PSD), which describes how the power of a signal or time series is distributed over the different frequencies. The power of a signal $u(t)$ can be defined as:

$$P = \lim_{T \to \infty} \frac{1}{T} \int_{0}^{+\infty} u(t) dt \tag{2.32}$$

for many signals of interest this Fourier transform does not exist. Because of this, it is advantageous to work with a *truncated Fourier transform* $\mathcal{F}_T(\omega)$, where the signal is integrated only over a finite interval:

$$\mathcal{F}_T(\omega) = \frac{1}{\sqrt{T}} \int_{0}^{+\infty} u(t) e^{-i\omega t} dt \tag{2.33}$$

The power spectral density can then be defined:

$$S_{uu}(\omega) = \lim_{T \to \infty} <\mathcal{F}_T(\omega)> \tag{2.34}$$

One extremely important attribute of the PSD is that for a statistically stationary process, it constitutes a Fourier transform pair with the autocovariance function $R(\tau)$ (Wiener-Khinchin theorem):

$$S_{uu}(\omega) = \frac{1}{2\pi} \int_{-\infty}^{+\infty} e^{-i\omega\tau} R(\tau) d\tau \tag{2.35}$$

The *inverse transform* is:

$$R(\tau) = \int_{-\infty}^{+\infty} e^{i\omega\tau} S_{uu}(\omega) d\omega \tag{2.36}$$

For $\tau = 0$, 2.36 becomes:

$$\overline{u^2} = \int_{-\infty}^{+\infty} S_{uu}(\omega) d\omega \tag{2.37}$$

So $S_{uu}(\omega)$ it can be interpreted as the variance (or turbulent energy) present in the band of legth $d\omega$ centered at ω. It is important to note that the power spectral density is an even function i.e. $S_{uu}(\omega) = S_{uu}(-\omega)$ but for our application we will only deal with positive frequencies, hence we will use the following

expedient:

$$P_{uu}(\omega) = 2S_{uu}(\omega) \tag{2.38}$$

if ω is positive, $P_{uu}(\omega) = 0$ otherwise.

2.2.7 Spectral density estimation in turbulent flows

When carrying out spectral analysis on experimental data, we want to estimate the spectral density of a random signal $u(t)$ from a finite sequence of time samples. The most obvious way to proceed would be to apply a discrete fourier transform (DFT) to the entire data set, also known as the periodogram method. This however gives many problems: first the spectral bias that is caused by the abrubt trucation of the data, a finite data set can in fact be seen as a signal multiplied by a rectangular window function. Furthermore this method would give an unacceptable random error and is proved that the variance of the estimated spectral density at any frequency does not diminish with the increase of data points. To reduce the spectral bias, a window function that provides a more gradual truncation of the data set is needed. The side effect is that when using a window a loss factor is introduced because part of the data is artificially damped. Then in order to reduce the random error and obtain a converging spectral density with sampling time, the signal can be divided in multiple segment where the DFT is computed separately, then the results are averaged. This is known as Bartlett's method (1948) and gives a smoother and more accurate PSD estimation but at the price of a reduced frequency resolution. For current measurements, the method proposed by Welch (1967) was used. It is an improvement on Bartlett's method. This method has the advantage of obtaining a smooth PSD estimate by computing the DFT for different data segments and then averaging them, but it also reduces the loss of information related to windowing by overlapping these segments. The method can be summarized in these steps:

- the sampled data of n points is divided into N segments, of length D, overlapping each other of a number of points equal to $D/2$ (50% overlap in this case)
- the individual N data segments have a window $w(t)$ applied to them (a simple Hanning window in this case) in the time domain to reduce bias
- DFT is calculated for $u(t)w(t)$ separately for every segment, then the square magnitude is computed, obtaining N spectral estimates

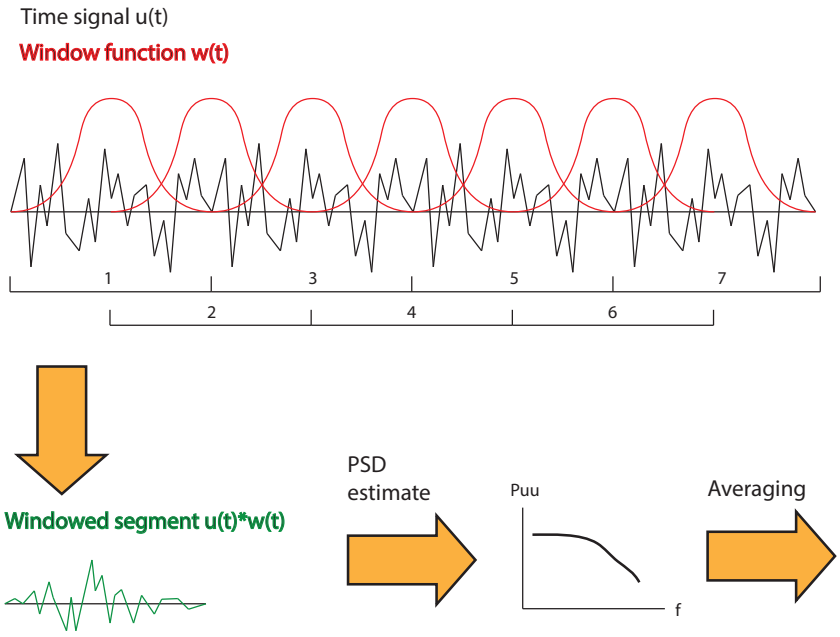

Figure 2.4: Welch's PSD method

- averaging is applied across the N PSD estimates to obtain the final result

Figure 2.4 gives an idea of the procedure applied to the data.

2.3 Jet flow

A jet flow is produced everytime fluid is ejected trough a round nozzle. A simple schematic of a round jet flow is shown in figure 2.5, the x axis is coincident with the nozzle symmetry axis, D is the nozzle's exit diameter. Let's make the assumption that the flow is statistically stationary; given the axisymmetric nature of the flow, statistics depend on the axial and radial coordinates, x and r, but not on the circumferential coordinate θ or on the time. The velocity components in the x, r and θ direction are, respectively, U, V and W. To characterize the flow we use the following Reynolds number:

$$Re = \frac{U_j D}{\nu} \tag{2.39}$$

Where U_j is the axial velocity immediatly at the nozzle exit ($x = 0$), which is almost a constant flat-topped velocity profile. In reality the velocity profile obtained at the nozzle's exit greatly depends on the characteristics of the nozzle

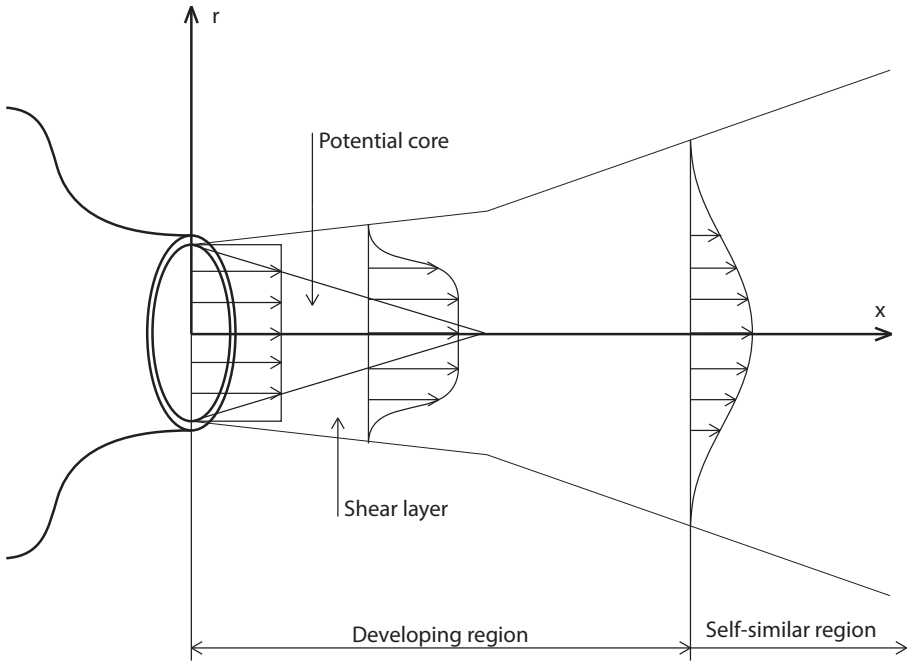

Figure 2.5: Jet schematics

itself. For example a nozzle with a big contraction ratio (the ratio between the initial and final diameter of the nozzle) will produce an almost constant velocity profile, while for nozzles with a lower contraction ratio the velocity profile is different. Furthermore also the surrounding ambient plays an effect on the jet, as discussed by Hussein et al (1994), and the jet must be far enough from surrounding walls to be considered with good approximation as a jet in an infite enviroment. The area immediately behind the nozzle lip is characterized by a strong velocity gradient, as the air ejected from the nozzle at a velocity close to U_j encounters the still ambient air; this causes a shear layer to form and develop along the x-axis between the ambient air and the jet. In the near-field region of the jet the initial inviscid *potential core* is gradually replaced by the growing shear layer until, at about a distance of six diameters from the exit (Lee & Chu 2003), the shear layer reaches the centerline and completely engulfs the core region. During this phase the initial top-hat profile of $\overline{U}(x, r)$ is gradually changed as the core grows thinner, in a core region-mixing layer profile. After $6D$ there is *development region* that covers approximately $0 < x/D < 20$, where the mean axial velocity profile keeps changing until, at about twenty diameters

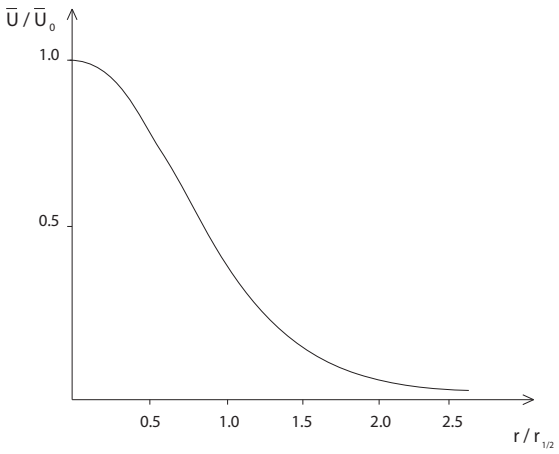

Figure 2.6: Mean axial velocity profile normalized by the mean centerline velocity, as a function of $r/r_{1/2}$ in the self-similar region of the jet.

from the exit the velocity profile assumes its characteristic gaussian shape. It is then said that the mean vesocity profile reaches a *self-preserving shape* or that the profiles from 20 D onwards are *self-similar*. As could be expected, the mean velocity is predominantly in the axial direction, the mean circumferencial velocity $\overline{W}$ is zero, while the mean radial velocity $\overline{V}$ is one order of magnitude smaller than $\overline{U}$. Two observation can be made by looking at the axial mean velocity profile at different points down stream. One is that the jet spreads radially with increasing x values, the other is that $\overline{U}$ decays over time. It can be seen because the $\overline{U}(x,r)$ profile grows wider but flatter with increasing x/D values. It is interesting to note that beyond what was previously referred to as *development region*, altough the jet continues to spread, the shape of the mean axial velocity profile $\overline{U}(x,r)$ remains the same. Infact if we define $r_{1/2}(x)$ as the radial coordinate for which, at a specific x value the mean value of the axial velocity is half of that for $r = 0$, $\overline{U}_0(x)$:

$$\overline{U}(x, r_{1/2}) = \frac{1}{2}\overline{U}(x, 0) \tag{2.40}$$

If now we plot $\overline{U}(x,r)/\overline{U}(x,0)$ against $r/r_{1/2}$ all the different mean velocity profile curves collapse on the same one (figure 2.6). This brings to the important conclusion that after the development region, the velocity profiles become *self-similar*. If we consider the behaviour of the mean axial velocity at the centerline, $\overline{U}_0(x)$ we can see that it decays linerly downstream, as can be seen in figure 2.7 where $\overline{U}_0(x)$ is plotted against x/D. To describe analitically this fact, the

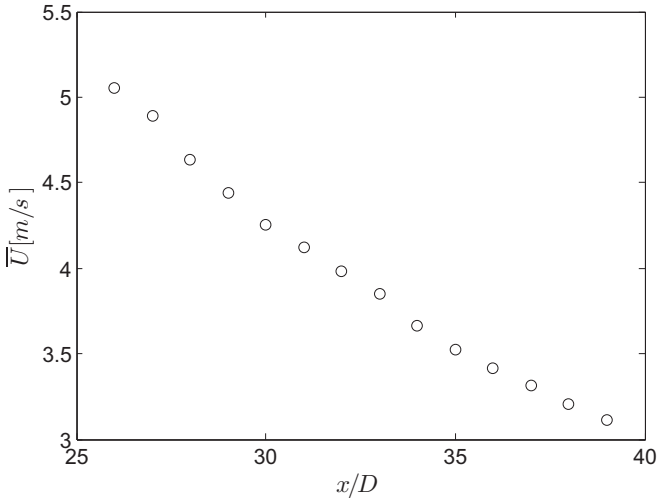

Figure 2.7: Mean axial velocity on the jet centreline, as a function of x/D in the self-similar region of the jet, from current measurements.

following expression can be used¡:

$$\frac{\overline{U}_0(x)}{U_j} = \frac{B}{(x - x_0)/D} \tag{2.41}$$

Where the parameter B is an empirical constant, and defines the speed at which the mean axial velocity decays over space. Also the the spreading of the jet into the undisturbed fluid is found to have a linear behaviour in the self-similar region. In other words, the *spreading rate* S, defined as:

$$S = \frac{dr_{1/2}}{dx} \tag{2.42}$$

is a constant. We can write the law that governs the change in $r_{1/2}$:

$$r_{1/2}(x) = S(x - x_0) \tag{2.43}$$

It is important to note that these linear behaviours do not hold in the development region of the jet. In regards to the flow one may ask what is the influence of the Reynolds number on the mean axial velocity statistics and flow development; in this case it has been experimentally verified that the velocity-decay constant B, the spreding rate S and the shape of the mean velocity profile in the self-similar region are all independent on the Reynolds number; in particular the jet spreads in this region with an angle of approximately 26°. For

what concerns the lateral velocity $\overline{V}(x,r)$ in the self-similar region, it could be found from the continuity equation equation knowing $\overline{U}(x,r)$. Figure 2.8 shows a profile of the mean lateral velocity. It shows that in the first part of the jet its sligthly positive, while it becomes sligthly negative further away from the centerline, signalling the fact that while at first is the air coming from the jet and expands into the ambient; then it's the ambient air that enters and gets *entrained* in the jet. The mean lateral velocity is however more than one order of magnitude smaller that the axial one.

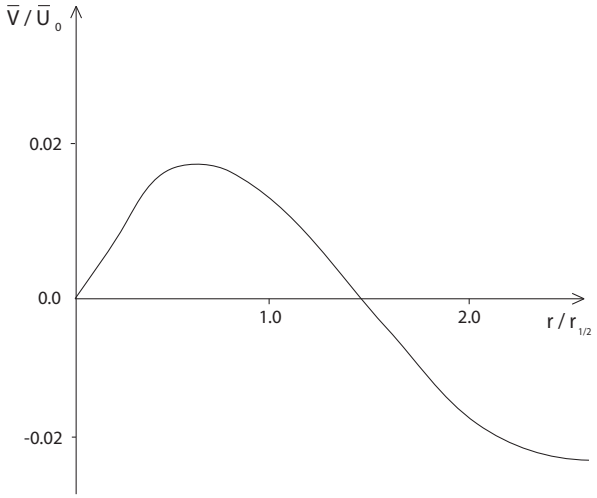

Figure 2.8: Mean lateral velocity profile normalized by the mean centerline velocity, as a function of $r/r_{1/2}$ in the self-similar region of the jet.

Chapter 3

Hot-wire anemometry

3.1 Introduction

Hot-wire anemometry (HWA) remains, many years after its first introduction by King (1914), the leading technique for velocity measuraments in the field of turbulent flows. The reason for it being that, with a careful design of the sensor and anemometer system, spatial and temporal resolution exceeding the ones of the other widespread measurament techniques can be achieved, making it an unvaluable tool for turbulence investigation. The basic principle of hot-wire anemometry is that a heated body (a very fine wire in our case) in a flow will experience a cooling effect. This effect is mainly associated to forced convection heat losses (but not only, as we will see later) which are strongly velocity dependant. If is in some way possible to measure this heat loss, then, by means of an accurate calibration, it would be possible to retrieve the flow velocity based on the wire's cooling rate. In the hot-wire case this cooling effect can be measured either by measuring the change in temperature of the sensor (costant current anemometer) or either by measuring the action necessary to keep it at a constant temperature (costant temperature anemometer). This section will provide a general description of hot-wire anemometry and its main features. For a more in-depth review it is recommended to refer to classical literature on the subject, which is extremely vast and comprehensive, including Perry (1982), Lomas (1986), Bruun (1995) or more recently Tropea *et al* (2007).

3.1.1 Main advantages and disadvantages of HWA

Hot-wire anemometry has many advantages over other measuring techniques, which have made it very popular in turbulent flow measuraments:

- Relatively low cost, for the probe and anemometer system, if compared to Laser Doppler Anemometry (LDA).
- A hot-wire, when used in conjunction with a Constant Temperature Anemometer (CTA) has an unfiltered frequency response up to 50 kHz, while LDA measuraments are usualy limited at less than 30 kHz.
- Hot-wires, thanks to their very small physical dimensions, have a small measuring volume and therefore an extremely good spatial resolution.
- Temperature measuraments are possible, if the wire is operated as a *cold wire.*

On the other hand hot-wire anemometry also presents a number of "problems" which must be acknowledged and adressed in order to obtain reliable results:

- The method is intrusive, and while the wire itself is very small, the other probe parts may not, and so they can disturb the flow in the vicinity of the wire. This of coure is not a problem with LDA.
- Hot-wires are limited to low and medium intensity turbulence flows, the problem being that a reverse flow can't be recognized and in high turbulence flows the velocity vector may fall outside of the acceptance cone
- They have consistent drift over time, may be affected by contamination and their response is higly dependant on ambient quantities (Temperature being the dominant one). For this reason frequent calibrations are necessary.
- Hot-wires are intrinsecally fragile; and the smaller they are the more brittle they become. For this reason even trivial procedures like mounting the probe on its support can become the cause for breakage. Also the presence of very small particles in the flow may result in a wire breakage, if there is an impact between the two.

3.2 Sensor material and geometry

In a hot-wire anemometer, the sensing element is constituted by a very fine wire exposed to the incident flow, with lenght ranging from 0.5 to 2 mm and diameters from 0.6 to 5 microns. A list of typical material used for wires with their properties is reported in table 3.2: As we will see more in detail later, a

Material	Resistivity	Temperature coefficient α	Specific heat c_w	Thermal conductivity k_w
Platinum	$1.1 * 10^{-7}$	$3.9 * 10^{-3}$	130	70
Pt - 10% Rh	$1.9 * 10^{-7}$	$1.7 * 10^{-3}$	150	40
Tungsten	$0.6 * 10^{-7}$	$4.5 * 10^{-3}$	140	170

Table 3.1: Typical wire materials and their properties

small physical lenght of the wire permits to achieve a better spatial resolution, as smaller scale fluctuations can be measured. On the other hand however, a high aspect ratio of the wire (l/d) must be maintained, to ensure that conduction of heat from the wire to the supports can be neglected compared to the heat lost by forced convection. Typical values of l/d are around 200. This two contradicting requirements lead to the fact that to achieve a good spatial resolution (necessary for turbulence measuraments) and maintain an acceptable l/d ratio, one ends up using very small diameter wires (down to 0.6 micron) with the consequences of having a very brittle and fragile sensor. The wire is physically attached to needle shaped supports, known as *prongs*, which can be 5 - 10 mm long and have a diameter of 0.5 - 0.3 mm, near the end they are usually mechanically or chemically tapered to minimize aerodynamic interference to the wire. The function of the prongs is to provide support to the wire ad act as an electrical connection to the rest of the probe. Very thin and long prongs can ensure a very low level of disturbances (see Comte-Bellot *et al* (1971) for a comprehensive study on aerodynamic interferences acting on a hot-wire), but at the cost of a loss in stiffness; which may cause problems if the wire is subject to a high velocity, because the prongs bend slightly (this is particularly true for boundary-layer probes, whose prongs are not parallel to the flow). Some times the sensor does not span the entire distance between the prongs. There can be an inactive part of the wire close to the prongs that does not participate in the sensor response. This part is called *stub* . For platinum wires obtained with the Wollaston process, the stub is a portion of wire which has not been etched, and still retains its silver coating.

3.2.1 Probe geometry types

Hot-wire sensors are commercially available in different configurations, with one, two or more sensor wires. A sensor response depends on both magnitude and direction of the incident velocity vector, so more sensor wires placed at different

angles with respect to the incident velocity, can be used to obtain information on the fluid's velocity direction.

- Single sensor probes, shown in figure 3.2a are used for one-dimensional, uni directional flows. The wire is mounted perpendicular to the flow direction and the prongs parallel to it. It is important to note that the wire can't determine the orientation of the velocity vector, and velocity should always be positive to avoid rectification errors. therefore the mean velocity has to be different than zero, and the turbulence fluctuations of such a magnitude to avoid a reverse flow.

- Dual sensor probes shown in figure 3.2c; also called X-type probes, are made of two inclined wires lying in the $x - y$ plane (see the probe reference system in figure 3.1) and often placed symmetrically relative to the longitudinal velocity component U_x. The midpoints of both wires are slightly separated along the z axis in order to reduce aerodynamic and thermal interferences. They can be used to determine two components of the fluid's velocity. The velocity vector must always be positive with respect to each wire, and this defines the acceptance cone; if the two wire are mutually orthogonal this angle is 90°. Another type of dual sensor probe, called V probe, is used when two component measurements have to be made close to the wall, and the spatial resolution in the y-direction is of extreme importance. Therefore the two wires are placed one next to the other instead of one over the other.

- Triple sensor probe shown in figure 3.2d; They have a rather complex prongs geometry with three mutually orthogonal wires. Intended for three dimensional flows, they are able to provide information about the istantaneous velocity at a point, with all its components U_x, U_y and U_z. The acceptance cone is reduced to 70°.

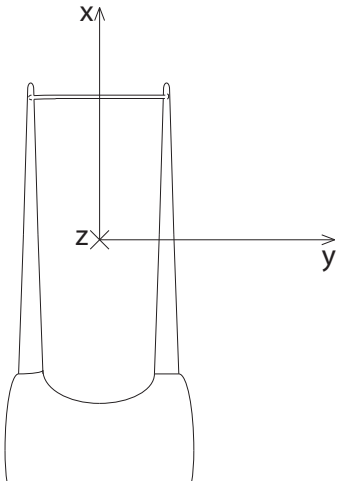

Figure 3.1: Probe reference system.

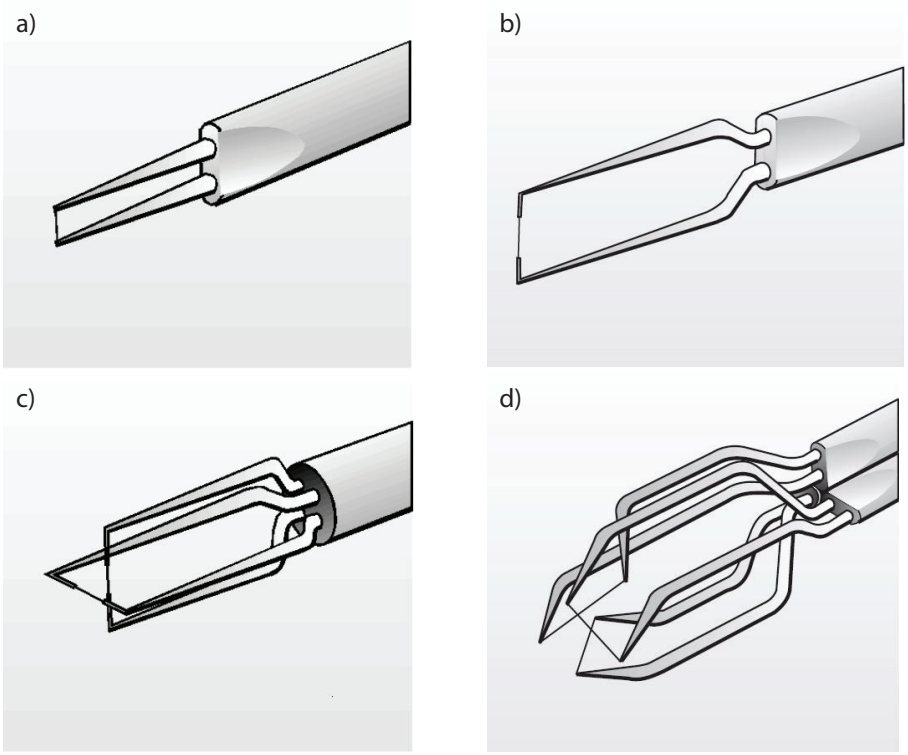

Figure 3.2: Different types of commercial hot-wire probes: a) single wire probe, b) stubbed single wire probe, c) x-wire probe, d) three-wire probe. (From Jorgensen (2002)).

3.3 Governing equations

We will now have a look at how heat is generated and lost in a hot-wire. In the most general case of an unsteady flow condition (which is indeed always the case when the flow is turbulent), we can write this relation:

$$m_w c_w \frac{dT_w}{dt} = W - Q \tag{3.1}$$

The left hand term represents the change in heat energy stored in the wire, where T_w is the wire's temperature, m_w is its mass and c_w is the specific heat of the wire's material. In the right side of the equation, W is the power produced and Q is the power dissipated by the wire. In hot-wire anemometry, the heating is achieved by means of Joule effect: a current I_w is passed throught the wire, and the power dissipated is equal to $I_w^2 R_w$, where R_w is the wire's electrical resistance (which, is important to stress, is dependant on the wire's temperature T_w).

$$W = I_w^2 R_w \tag{3.2}$$

On the other hand, neglecting for the moment other forms of heat losses, we have that the heat lost per second due to forced convection (which in most flow cases is by far the dominant one) is given by:

$$Q = (T_w - T_a) A h(U) \tag{3.3}$$

where T_a is the temperature of the fluid that is in contact with the wire, A is the surface area over which forced convection takes place, and h is the forced convection heat transfer coefficient which is dependant, amongst other things, on the fluid velocity normal to the wire. Studying the stationary case the heat storage term on the left side of (3.1) is equal to zero (given the extremely low thermal inertia of the wire, the equilibrium is hastily reached). At the equilibrium holds:

$$I_w^2 R_w = (T_w - T_a) A h(U) \tag{3.4}$$

Now, if we remember that R_w can be expressed a function of T_w, using a linear approximation around a certain reference temperature T_0, we can write:

$$R_w = R_0[1 + \alpha_0 (T_w - T_0)] \tag{3.5}$$

where R_0 is the wire resistance evaluated at temperature T_0 and α_0 is the resistivity coefficient of the wire material at the same temperature. For metals

this value is positive, meaning that resistance increases with increasing temperature. If we take the fluid ambient temperature as our reference temperature, it's possible to derive the following expression:

$$T_w - T_a = \frac{R_w - R_a}{\alpha_a R_a} \tag{3.6}$$

A very important parameter defining the sensor operating point is the so called overheat ratio a_w, which is the relative difference in resistance between the wire at operating and ambient(flow) temperature:

$$a_w = \frac{R_w - R_a}{R_a} \tag{3.7}$$

A higher overheat ratio grants a greater velocity sensitivity of the sensor. Usually overheat values are limited to avoid sensor oxidation or deformation. A typical value for tungsten wire anemometers is 0.8, meaning that resistance is increased by 80% compared to its ambient temperature value.

3.3.1 Convective Heat Transfer

In the case of a cilinder-shaped body, the forced convection coefficient h can be expressed as:

$$h = \frac{Nu\, k_f}{d_w} \tag{3.8}$$

where k_f is the thermal conductivity of the fluid, and d_w is the cilinder's diameter. Nu is the Nusselt's number, which is itself a function of many parameters:

$$Nu = Nu\left(M, Re, Gr, Pr, \gamma, \frac{T_w - T_a}{T_a}\right) \tag{3.9}$$

wich are, in order: the Mach, Reynolds, Grashof and Prandtl numbers, the ratio between specific heat at costant pressure and volume, and the wire temperature difference. Some of this parameters are defined as

$$M = \frac{U}{c} \tag{3.10}$$

$$Re = \frac{U d_w}{\nu} \tag{3.11}$$

$$Gr = g\beta(T_w - T_a)d_w^3\nu^2 \tag{3.12}$$

$$Pr = \frac{c_p \nu}{k_f \rho} \tag{3.13}$$

Where k_f, ρ, μ and ν are the cofficient of conduction, the density, the dynamic and cinematic viscosity of the fluid. The physical properties of the fluid are either evaluated at ambient temperature T_a or at the so called film temperature T_f, which is defined as $(T_a + T_w)/2$, and is an approximation of fluid's temperature in the immediate vicinity of the wire. It's important to remark that the Reynolds number which is significant for the Nusselt number is the one of the wire, which uses as the characteristic lenght the wire diameter d_w; from now on it will be referred as Re_w to avoid confusion. Usually $2 < Re_w < 40$ for hot-wires measurements, well before the onset of vortex shedding. If we consider subsonic air flows, which is the standard for turbulence investigation, γ and Pr can be considered constant, in absence of compressibility effects the Mach number can be neglected and, if the heat exchange is dominated by forced convection (which is the case for hot-wires), even the dependancy on the Grashof number can be neglected. So equation (3.9) becomes:

$$Nu = Nu\left(Re_w, \frac{T_w - T_a}{T_a}\right) \tag{3.14}$$

A lot of different correlation expressions exist in literature regarding the Nusselt number, they usually share the form

$$Nu = A_1 + B_1 Re_w^n \tag{3.15}$$

Where A, B and n (which is usually taken 0.5) are characteristic constants of the particular correlation function. Considering a specific wire diameter, Re_w can be considered a function of only the velocity U, and the (3.15) can be rewritten as:

$$Nu = A_2 + B_2 U^n \tag{3.16}$$

Combining equations (3.4), (3.6) and (3.16) one can obtain the so called King's law:

$$\frac{I_w^2 R_w}{R_w - R_a} = A + BU^n \tag{3.17}$$

Introducing the voltage across the hot-wire, $E_w = I_w R_w$ and using relation (3.6) , equation (3.17) becomes:

$$\frac{E_w^2}{R_w} = (A + BU^n)(T_w - T_a) \tag{3.18}$$

Where the term α_0 was included in the costants A and B. keep in mind that this relation holds for the wire itself, and not for the anemometer output, wich obvi-

ously includes the additional resistance given by the probe and the anemometer circuit.

3.4 Anemometric circuit

In this section a brief description of different kinds of hot-wire anemometer circuitry corresponding to the different modes of operation will be provided. This description is intended to give a reasonable understanding of the electronics used in a hot-wire anemometer, without covering all the aspects and details of this subject, since that's not the aim of this thesis.

3.4.1 Constant current anemometer

Historically (from the early 1920s) the first mode of operation to be employed was the constant current mode, also known as CCA. Altought not necessary, the most pratical and effective way to use this technique is to insert the sensor in a wheatstone bridge, as in figure 3.3. After a specific overheat ratio has been selected, the wire resistance R_w can be retrieved, when the bridge is in balance, by the expression:

$$\frac{R_w + R_L}{R_1} = \frac{R_3}{R_2} \tag{3.19}$$

where R_3 is the adjustable resistance and R_L is the cable resistance, which icludes also connections and prongs resistance, with the only exception being the wire itself. In this mode of operation, during calibration, the current is kept at a constant value and the bridge is kept in balance by acting on the resistances R_L and R_3. The value of R_w is then calculated from equation (3.19). This procedures makes CCA laborious and cumbersome to use. Since the current I passing through the hot-wire is a known constant, it can be used in relation (3.17) and the calibration constants A and B can be retrieved, for example by a least-square fitting.

3.4.2 Constant temperature anemometer

This mode of operation has become popular later than the constant current mode, but presents many advantages and is currently the method that is universally used for turbulent velocity measurements. Since the wire is kept at a constant temperature (and therefore resistance), its thermal inertia doesn't limit anymore the frequency response of the system, allowing for a much better tracking of the high frequency turbulent fluctuations. This requires however a more

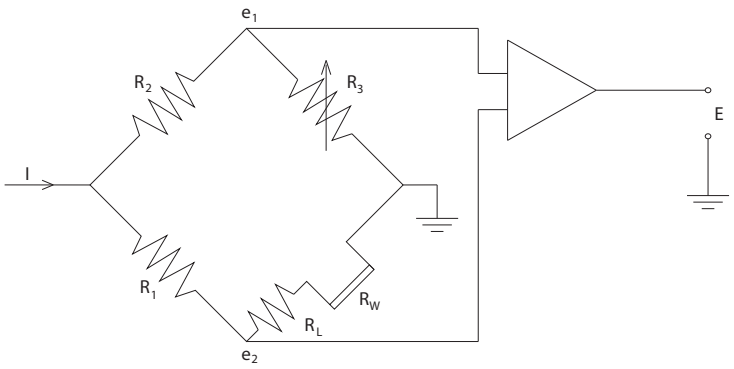

Figure 3.3: CCA circuit

complex circuit, as a feedback mechanism must be present in the anemometer circuit, that allows for extremely fast variations in the heating current of the wire I. Althought advantages of the CTA were theorized al early as the late 40s, it was not until the mid 60s that the progress in electronics allowed this mode of operation to be used. An example of a CTA circuit is shown in figure 3.4, with

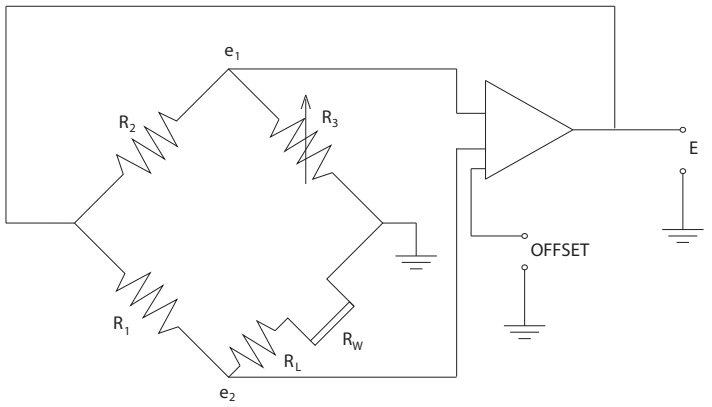

Figure 3.4: CTA circuit

a feedback differential amplifier. The hot-wire itself is placed in a Wheatstone bridge, just like in the CCA mode of operation; as the flow velocity varies, the wire's temperature varies, and so does its resistance R_w. The voltages e_1 and e_2 are the inputs of the differential amplifier, and their difference is a measure of how much the wire's resistance has changed. The output current of the amplifier is inversely proportional to $e_2 - e_1$, and is fed on the top of the bridge, restoring the wire's nominal resistance (and temperature). Modern feedback mechanism

are extremely fast and readily available in commercial CTA. These CTAs generally allow for some changes in settings such as: offset voltage, amplifier gain, low-pass filter parameters and so on.

3.5 Velocity calibration

The aim of the calibration procedure for a hot-wire sensor and its anemometer is to establish the relationship between the anemometer output voltage and the magnitude and direction of the incident velocity vector. In fact, despite the theoretical description given in the previous section, an analytical expression that relates the voltage across the hot-wire with the istantaneous flow velocity and takes everything into account does not exist. For this reason each hot-wire probe has to be calibrated before measurements by exsposing it to a set of known velocities. In order to obtain the transfer function that converts voltage data into velocities, a calibration curve has to be fitted to the calibration points. Typical calibration curves include King's law:

$$E^2 = A + BU^n \tag{3.20}$$

King identified n's value with 0.5 but later it was proved that a sligtly lower value works better. Also polynomial fitting might be used; a very common calibration expression is a fourth order polynomial relation:

$$U = C_0 + C_1E + C_2E^2 + C_3E^3 + C_4E^4 \tag{3.21}$$

Where C_0 to C_4 are the calibration constants to be determined. Despite not having any physical basis, polynomial fitting allows for a very high accuracy with a small linearization error. It works very well when high number of calibration points have been acquired but falls short when the velocities are outside the calibration ones, for example for low velocities. In this case the King's law remains a better solution, thanks to its physical basis, as it utilizes Newton's law of cooling that relates joule heating and forced convection. Because of this though, it may lead to some error when forced convection is not the sole phenomenon causing cooling on the wire, for example for very low velocities, where natural convection becomes relevant. A modified version of King's law was proposed by Johansson & Alfredsson (1982) and takes natural convection into account:

$$U = k_1(E^2 - E_0^2)^{1/n} + k_2(E - E_0)^{0.5} \tag{3.22}$$

Where E_0 is the voltage across the wire with a zero flow velocity.

3.5.1 Temperature compensation

It is very important to keep track of the flow temperature during calibration and experimental measures. The reason being that thermal exchange caused by forced convection is directly proportional to the difference between the wire and the ambient (flow) temperature ($T_w - T_a$), as can be seen in expression (3.3); a temperature deviation of 1°C may lead to a velocity error of around 2%. Because of this, we have to take temperature into account if we use a sensor in a flow whose temperature differs from the one of its calibration or if the temperature changes during the calibration itself. If a hot-wire is used to measure velocity at a higher flow temperature than its calibration, the heat dissipated via forced convection will be lower, and so will the velocity reading. In order to retrieve the correct velocity a compensation for temperature variations is required. If calibration has been carried out at a reference temperature T_{ref}, an analytical correction must be used to retrieve the correct voltage output at the operating flow temperature T_a:

$$E(T_{ref})^2 = E(T_a)^2 \frac{T_w - T_{ref}}{T_w - T_a} \tag{3.23}$$

where T_w is the wire's temperature and its fixed if the sensor is operating in CTA mode, $E(T_a)$ is the output voltage and $E(T_{ref})$ is the compensated output voltage. We can rewrite the compensation expression using the overheat ratio a_w and the temperature coefficient of electrical resistivity α:

$$E(T_{ref})^2 = E(T_a)^2 \left(1 - \frac{T_a - T_{ref}}{a_w/\alpha}\right)^{-1} \tag{3.24}$$

These parameters are known from the material properties and the anemometer's settings, are are more easily used than the wire's operating temperature T_w. Obviously to employ this correction method, a temperature sensor is needed to measure the flow temperature.

3.6 Temperature distribution in a finite wire

The purpose of a hot-wire is to measure velocity by measuring the cooling caused by the incident flow via forced convection; unfourtunately this isn't the only thermal exchange happening, heat is also transferred by conduction from

the wire to the prongs, partecipating in the cooling. This however represents an undesirable side-effect, to be kept as little as possible. In this section a more in-depth description of the phenomenon will be given, mainly following the text of Bruun (1995) and Tropea *et al* (2007). We may consider a small element of wire of lenght dx, depicted in figure 3.5 and write a heat balance equation:

$$d\dot{Q}_w = d\dot{Q}_{el} - d\dot{Q}_{fc} - d\dot{Q}_c - d\dot{Q}_r \tag{3.25}$$

Where $d\dot{Q}_{el}$ is the heat generation rate caused by Joule effect, $d\dot{Q}_{fc}$ is the heat dissipation rate due to forced convection, $d\dot{Q}_c$ is caused by conduction to neighbouring wire elements and $d\dot{Q}_r$ by radiation. $d\dot{Q}_w$ is the thermal energy stored in the wire element. We may express the terms in (3.25) as:

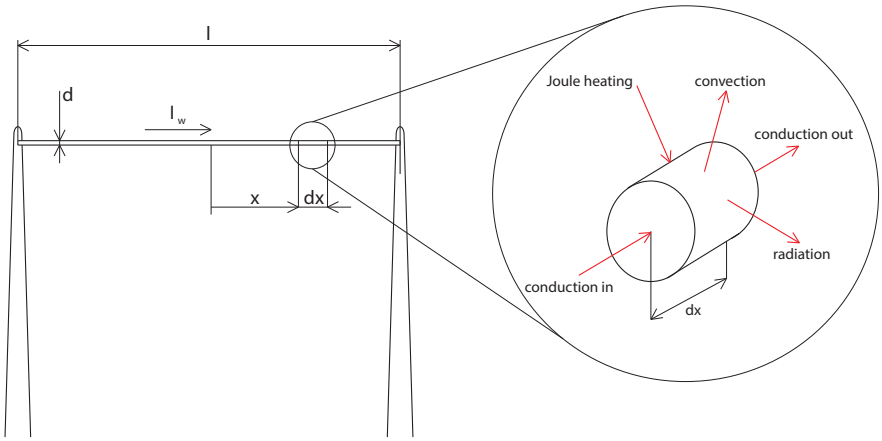

Figure 3.5: Heat exchanges in a hot-wire element

$$d\dot{Q}_{el} = \frac{I_w^2 \chi_w}{A_w} dx \tag{3.26}$$

where I_w is the current passing trought the wire, χ_w is the wire's resistivity at temperature T_w, and A_w is the wire's section area.

$$d\dot{Q}_{fc} = \pi d_w h (T_w - T_a) dx \tag{3.27}$$

where d_w is the wire diameter, T_a is the ambient temperature and h is the coefficient of forced convection.

$$d\dot{Q}_c = -k_w A_w \frac{\partial T_w^2}{\partial^2 x} dx \tag{3.28}$$

where k_w is the thermal conductivity of the wire; the higher the aspect ratio of the sensor l/d, the lower the dissipation by conduction is.

$$d\dot{Q}_r = \pi d_w \sigma \epsilon (T_w^4 - T_s^4) dx \tag{3.29}$$

where σ is the Sefan-Boltzmann constant, ϵ is the emissivity of the wire and T_s is the temperature of the surroundings. This term is usually very small and can be neglected.

$$d\dot{Q}_w = \rho_w c_w A_w \frac{\partial T_w}{\partial t} dx \tag{3.30}$$

where c_w is the specific heat per unit mass of the wire, and ρ_w is its density. By inserting equations (3.26)-(3.30) into (3.25), we get:

$$\rho_w c_w A_w \frac{\partial T_w}{\partial t} = + \frac{I_w^2 \chi w}{A_w} - \pi d_w h (T_w - T_a) + k_w A_w \frac{\partial T_w^2}{\partial^2 x} - \pi d_w \sigma \epsilon (T_w^4 - T_s^4) \tag{3.31}$$

The resistivity of the wire's material is a funcion of temperature, and using a linear approximation can be expressed as:

$$\chi_w = \chi_a (1 + \alpha_a (T_w - T_a)) \tag{3.32}$$

Where χ_a is the resistivity at ambient temperature, and α_a is the temperature coefficient at the same temperature. If we consider the steady state case, T_w doesn't change over time, also we may neglect the radiation term and include (3.32) and we obtain

$$k_w A_w \frac{\partial^2 T_w}{\partial x^2} + \left(\frac{I_w^2 \alpha_a \chi_a}{A_w} - \pi d_w h \right) (T_w - T_a) + \frac{I_w^2 \chi_a}{A_w} = 0 \tag{3.33}$$

If we assume T_a to be a constant, we can express the previous relationship as:

$$\frac{\partial^2 T^*}{\partial x^2} + C T^* + D = 0 \tag{3.34}$$

where:

$$T^* = T_w - T_a \tag{3.35}$$

$$C = \frac{I_w^2 \chi_a \alpha_a}{k_w A_w^2} - \frac{\pi h d_w}{k_w A_w} \tag{3.36}$$

$$D = \frac{I_w^2 \chi_a}{k_w A_w^2} \tag{3.37}$$

This equation can be treated analitically if we assume to have a constant T_a, prongs much bigger than the wire which can be assumed to be at ambient temperature, and a steady (i.e. constant h), uniform and isothermal incident flow. Davies and Fisher (1964) derived the solution of this equation for a wire of lenght l;

$$T_w(x) = \frac{D}{C}\left(1 - \frac{cosh(|C|^{0.5}x)}{cosh(|C|^{0.5}l/2)}\right) + T_a \tag{3.38}$$

equation (3.38) gives the distribution of temperature along the wire of length l. We can compute the mean temperature of the wire $\overline{T}_w$:

$$\overline{T}_w = \frac{1}{l}\int_{-l/2}^{l/2} T_w(x)dx = \frac{D}{C}\left(1 - \frac{tanh(\sqrt{C}l/2)}{\sqrt{C}l/2}\right) + T_a \tag{3.39}$$

It can be shown that D/C is equal to $T_{w\infty} - T_a$ where $T_{w\infty}$ is the temperature of an ideal infinitely long wire (which is constant along the wire length), so we can rewrite (3.38) as:

$$\frac{T_w(x) - T_a}{T_{w\infty} - T_a} = 1 - \frac{cosh(|C|^{0.5}x)}{cosh(|C|^{0.5}l/2)} \tag{3.40}$$

The dimentionless parameter of the *Biot number* can be defined, It expresses the ratio between the heat-transfer coefficient of a solid at its surface and the heat conduction at the center of the solid; it should be as large as possible to favor the cooling of the wire by the incident flow.

$$Bi = \sqrt{C}l/2 \tag{3.41}$$

As we can see in figure 3.6, the higher the Biot number, the wider the length of wire which keeps an almost constant temperature in the centre. The heat dissipated by conduction to the prongs can be estimated from (3.28):

$$Q_c = 2k_w A_w \left|\frac{\partial T_w}{\partial x}\right|_{x=l/2} \tag{3.42}$$

the temperature derivative in $x = l/2$ can be calculated deriving (3.38), so the former becomes:

$$Q_c = 2k_w A_w D\frac{tanh(Bi)}{\sqrt{C}} \tag{3.43}$$

This is the heat lost per second due to conduction to the prongs, which in normal operating conditions of a hot-wire is better to keep it as small as possible; we

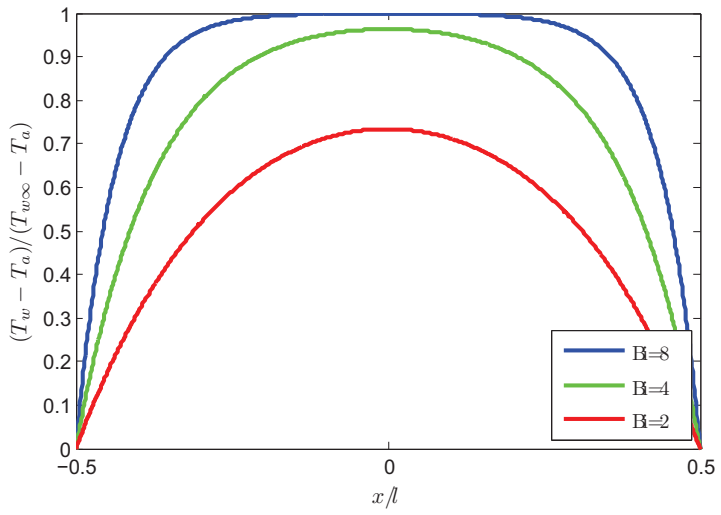

Figure 3.6: Temperature distribution for a finite wire, with different Biot numer cases

can compare it to the power generated with Joule heating; their ratio is:

$$\epsilon = \frac{Q_c}{I_w^2 R_w} = \frac{1}{1 + a_w} \frac{tanh(Bi)}{Bi} \tag{3.44}$$

Where a_w is as defined in (3.7). This equation can be plotted as a function of Bi. The heat exchanged from the wire to the prongs is also known as *end loss* and for most hot-wire measurements it represents 20% of the heat dissipated. The more the heat is lost via conduction, the less the sensitivity of the hot-wire to velocity fluctuations. To minimize the heat exchanged by conduction, one has to use a reasonably high Biot number (Bi depends both on sensor dimentions and on flow conditions) and a high overheat ratio a_w (the upper limit to the overheat ratio is set to avoid oxidation or damage of the sensor element). Generally this condition is summarized by stating that the wire's l/d ratio must be ¿ 200, but it is a semplification, as it also depends on flow conditions. It might not be enough, for example, in a boundary layer very close to the wall, where the mean velocity is extremely low. For this reason, Hultmark *et al* (2011) proposed a new parameter that includes wire's material properties and flow conditions.

3.7 Spatial resolution

Ideally we would like to be able to make velocity measurements in a point, this is however not possible as a consequence of the finite size of the sensor element, in our case the wire. Along the wire we might have a non-uniform distribution of velocities, this can be caused by two distinct phenomena: A difference in mean velocity, or a difference in instantaneous velocity. The first can occur in some particular flow fields, or can happen as a consequence of a wire misalignament (for example in a boundary layer). The second is an effect of the fine scales of turbulent flow and appears every time the wire length is not small compared to those scales. Here we will concentrate on the latter. Turbulent flows are charcterized by a large amount of different scales, from the large scales of length L, depending on the particular flow type and geometry, where the kinetic energy is introduced; to the smallest scales, the Kolmogorov scale η, where viscosity effects are dominant and the kinetic energy is dissipated. Although hot-wire sensors can be made very small, they still have a non negligible length, and if the smallest turbulent structures are smaller than the hot-wire, the sensor is not able to measure correctly the fluctuations of those scales (as depicted in figure 3.7). With the wire being unable to "see" the smaller velocity fluctuations, the effect on the measures is mainly a filtering and attenuations of the higher order statistics with a erroneously low turbulence intensity perceived. If we make the assumption that the cooling is given mainly by forced convection caused by the normal velocity component u, thus neglecting the tangential and bi-normal contribuition to forced convection, we get that the effective cooling velocity sensed by the wire is essentially given by the normal component, $U_{eff} \approx U$. If the normal velocity distribution along the wire is not constant, the istantaneous velocity reading will be a kind of spatial average of the velocity distribution along the wire. It is not strictly speaking a spatial average because the heat transfer is not linearly dependent on the effective velocity, taking King's law as an example:

$$\dot{Q} \propto A + BU^n \tag{3.45}$$

Under this assumption the "filtered" istantaneous velocity reading is:

$$u_m(t) = \left(\frac{1}{l} \int_{-l/2}^{l/2} U^n(s,t) ds \right)^{1/n} \tag{3.46}$$

Where l is the wire's length and s is the wire's coordinate centered on the wire mid-point. Here n denotes the non linear relation between the heat exchange

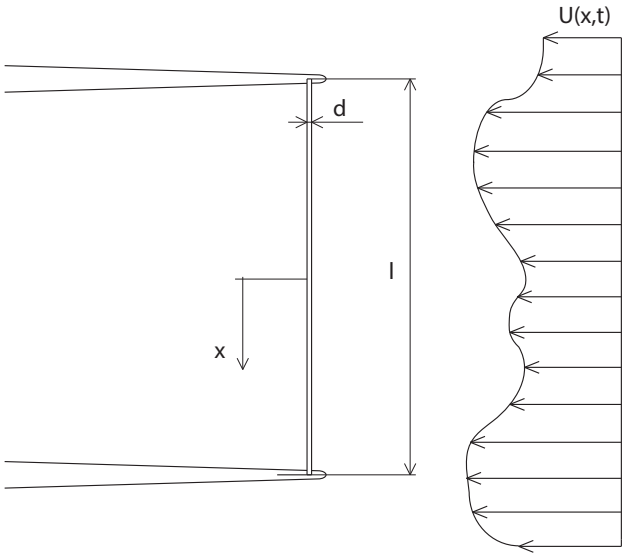

Figure 3.7: A hot-wire sensor with a non-uniform istantaneous incident velocity $U(x,t)$

and the velocity. The early theoretical work concerning hot-wire spatial resolution effects can be found in Dryden (1937) and Frenkiel (1949). Wyngaard (1968) calculated the effect of an incomplete spatial resolution on velocity spectra, using the local isotropy hypothesis and Pao's spectrum. Experimental work is mainly focused on wall flows, that is where spatial resolution effects are most visible. Ligrani and Bradshaw (1987 a,b) investigated the effects of wire's length on the statistics in the near-wall region of a boundary layer the attenuation, identifying the foundamental characterising parameters in the ratio l^+ but also l/d. More recently the subject was investigated by Hutchins *et al* (2009), and Örlü and Alfredsson (2009). Segalini *et al* (2011) and Smits *et al* (2011b) proposed correction schemes for spatial resolution errors.

Chapter 4

Hot-wire manufacturing

4.1 Introduction

Commercially made hot-wire probes are today available from several manufacturers, they are made of a welded tungsten wire with a length of at least 1mm and a diameter of 5μm, which ensures a, relatively speaking, robust and durable probe. The size of these sensors however, might pose a problem if small scale turbulence is the object of the experiment, because spatial resolution becomes a foundamental parameter. Another downside of the "off the shelf" hot-wire probes are the time and costs associated with repairing and delivering. The need for small sensors suitable for turbulence measurements has led many research groups to build their own sensors "in-house", as the relatively cheap and affordable material needed for their construction allows it. A smaller sensor is built using platinum wire that, although with lower mechanical properties, is available in diameters smaller than 5μm. Unlike the commercial welded probes, soft-soldering is used to attach the wire on the prongs. As a part of this thesis, a hot-wire laboratory was set up for the construction of sensors. A description of the manufacturing process and of the experimental apparatus used for hot-wire measurements will be provided in this chapter

4.2 Manufacturing procedure

4.2.1 Probe body

The probe body, sometimes referred to as *probe holder*, is made out of metallic tubes of different diameters. Different materials can be used, but in this specific case brass tubes were selected. One smaller $2.5x4.0mm$ and one $4.05x5.0mm$

tubes were used, the first inserted into the other. Their exposed edges were mechanically smoothed out in order to decrease any possible aerodynamic disturbances. Their purpose is to act as a housing for the inner part of the probe and to provide the attachment point of the probe on the traversing system. The length of the probe holder must be enough to keep the sensor element away from any possible aerodynamic interference generating from the traversing system. On the other hand an excessive length of this element can lead to the loss of flexural rigidity, with the result of having unwanted probe oscillations, expecially in high velocity flows. In this case a inner brass tube of 40 mm was inserted into a bigger outer one of 140 mm. Inside the inner tube of the probe holder a ceramic tube is used as a support for the prongs. It has an external diameter of 2.47mm, and two or four internal holes of 0.5mm of diameter that is where the prongs are placed. Ceramic is used as it ensures electrical insulation between the prongs and the metallic probe holder. In figure 4.1 is shown an assembled probe and its different internal parts.

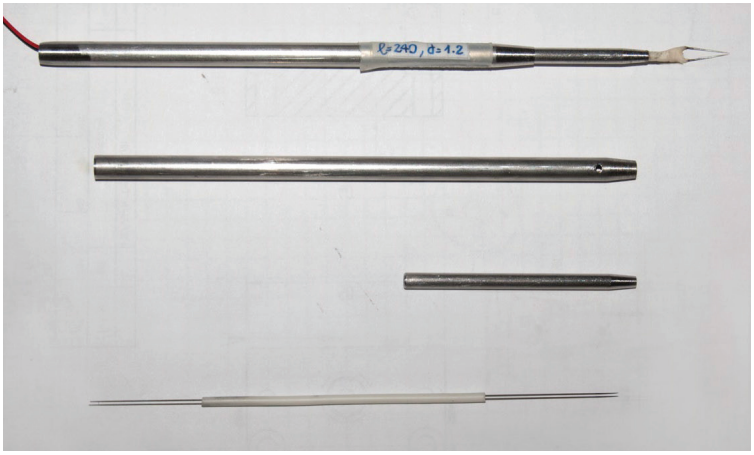

Figure 4.1: From top to bottom: a completed probe, the outer and inner probe holder (steel in this case), etched prongs inserted in their ceramic housing (Courtesy of Marco Ferro).

4.2.2 Prongs etching

One of the first operation to carry out is the etching of the prongs. The prongs are needle-like elements that serve as a support to solder the wire and also provide the electrical connection from the wire to the anemometer system. Steel piano wires with diameters ranging from 0.3 to 0.6 mm are used as prongs'

material. They must be etched near their ends, where the wire will be soldered, in order to obtain a more aerodynamically sound and less intrusive shape. This can be done mechanically with the help of appropriate tools, but a much better result can be achieved through *electroetching*. This technique involves the use of an electrolyte solution, an anode and a cathode. The metal piece to be etched is connected to the positive pole of a voltage source and acts as the anode, while another piece of metal is connected to the negative pole and is called cathode. To avoid unwanted electro-chemical effects, the anode and the cathode should be of the same metal. As the voltage source is turned on, the metal of the anode is dissolved and converted into the same cation as in the electrolyte solution and at the same time an equal amount of the cation in the solution is converted into metal and deposited on the cathode. In this case a 65% solution of nitric acid was used, the pair of prongs to be etched is attached to the positive pole while another prong acts as the cathode. In order to obtain the needle like shape that is needed the prongs have to be etched differentially, more on the tip and gradually less as we move away from it. This is achieved by moving alternatively the prongs in and out of the solution: the tip will stay immersed in the solution for a longer time compared with the portion of prongs further away from the tip, and when the prongs are completely out, the circuit is opened and etching does not take place. The more we move away from the tip the less time the material will spend in the solution. This produces an increasing degree of etching as we move downwards to the tip, ultimately resulting in the needle-shape. A special device, depicted in figure 4.2 was conceived and built for this purpose. It consists in a simple dc gear motor, speed adjustable, that drives a cam obtained from an eccentric disc. The cam in turn lifts a rod at the end of which the prongs are placed. The rod is hinged at one end to the device's housing, while under its free end a little becker containing a small amount of nitric acid solution is placed, just enough so that 3-4mm of the prongs can be immersed in it. The electric motor is contained in a plastic housing, and all the exposed part, hinge, rod and screws are also made of plastic. This is done to avoid corrosion to the parts exposed to acid exalations. During the electroetching process (see figure 4.3) metal clamps connected to the voltage source are attached to the prongs to be etched and to the piece of metal acting as the cathode. Then anode and cathode are immersed in the solution and the process can start. The operation must be carried out under a fume hood, as during the process toxic gas is released. The higher the voltage applied, the faster and more aggressive the etching is. Although appliying a higher voltage makes the process less

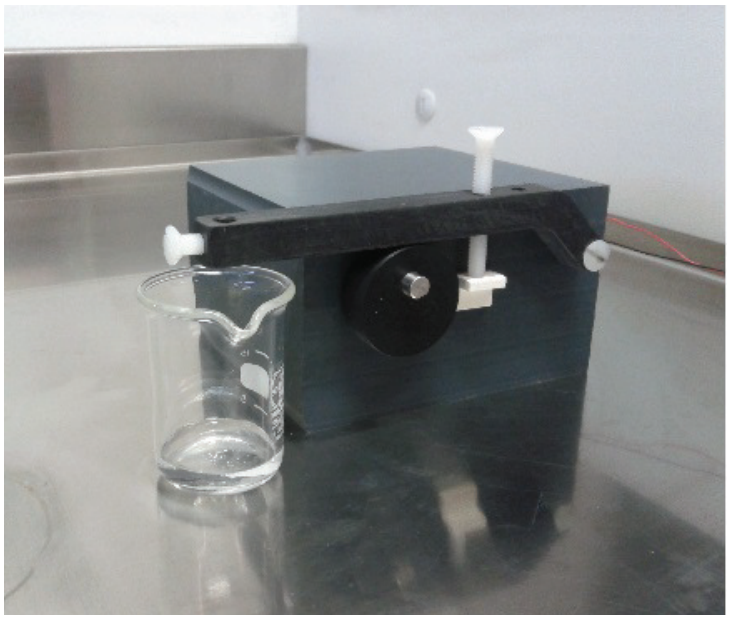

Figure 4.2: Device used for prongs etching, consisting in a simple cam and rod mechanism.

time-consuming, it also provokes bigger "chunks" of material do be removed at once, ultimately resulting in a worse surface quality. For this reason, a voltage of around 3-5 V was found to be a good compromise. With these voltage values, the etching takes no more that 6-7 minutes for the 0.5mm prongs. It is possible to momentarily discontinue the procedure and check the result with the microscope, and eventually change the voltage or reciprocating speed settings. The final result of the etching process was checked by placing the tip of the prongs under a microscope, if the result was not deemed satisfactory, they were discarded and the operation was repeated.

4.2.3 Prongs bending

After the prongs have been checked with the microscope, they are inserted into their ceramic housing, which in turn is glued inside the brass tube acting as the probe body. Then the prongs were bent in order to obtain boundary layer type probes. Even though to carry out jet measurements this is not necessary and simple probes with parallel prongs could have been used, it was decided tho shape them in this way because it's easier to make small adjustment on the prongs spacing and for the eventuality of a possible future use in wall flows. Two bends on different planes are made on each prong, using simple pliers. This operation may take some time, as a lot of little correction have to be made and

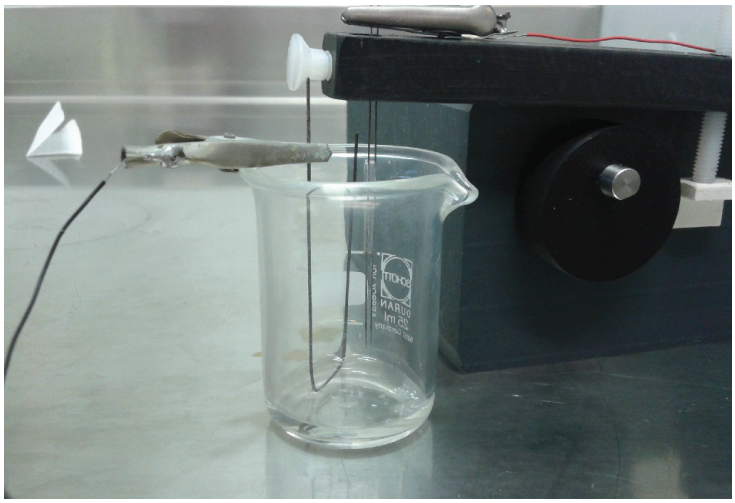

Figure 4.3: Metal clamps connected to a power source are attached to the anode (the prongs) and the cathode (a piece of a steel piano wire) during electroetching.

checked with the microscope each time, to ensure their effects. Strictly speaking, simmetry is not necessary (Although it might help). What is important is that the tip of the prongs are, referring to the probe's reference system (figure 3.1) at the same x and z coordinate, with their distance on the y axis corresponding exactly to the intended spacing. the x position of the prongs can be easily checked with the microscope, while for the spacing a feeler gauge is used and the blade with the appropriate thickness interposed between the prongs. The feeler gauge's blade between the prongs is observed with the microscope, to check the prongs' spacing (the blade should just be able to pass between the prongs, without bending them). As far as the z position is concerned, one way to check it is to slowly put into focus one of the prongs, if the other prong is not perfectly into focus when the other is, it means that its distance from the lens is slightly different and has to be corrected. When the prongs are in the intended position a drop of rapid glue is used to stick them in place. Then a bicomponent resin is applied between the ceramic tube and the prongs. The resin has two purposes: to provide a smooth ad aerodynamically sound transition between the probe body and the prongs and to support and strengthen the prongs. The resin is left to dry for a couple of hours and then it is shaped and the excess removed with a file until it assumes the desired shape (figure 4.4). After the resin dries up it can happen that the spacing between the prongs is sligthly reduced (the effect is more noticeable on smaller spacing prongs). In this case a little correction is needed. During the period of time spent at the KTH laboratories

in stockholm a progs-bending device (shown in figure 4.5 was built in order to have a fast way to obtain prongs with a repeatable shape. This helps a lot in the first phase of the bending, but prongs have to be adjusted nonetheless to obtain the desired spacing.

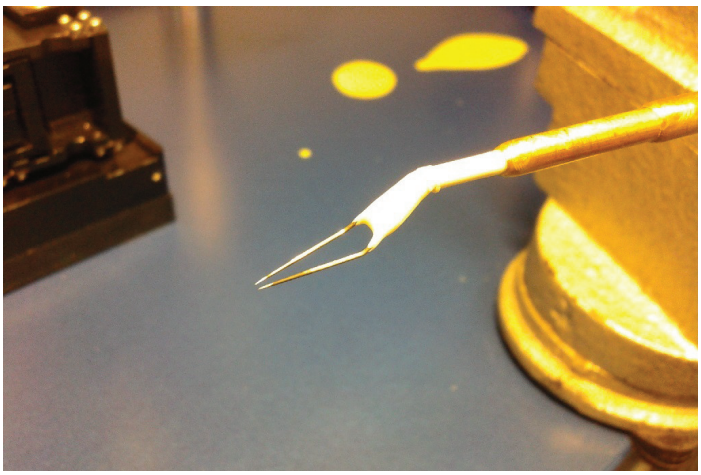

Figure 4.4: Example of boundary-layer type probe.

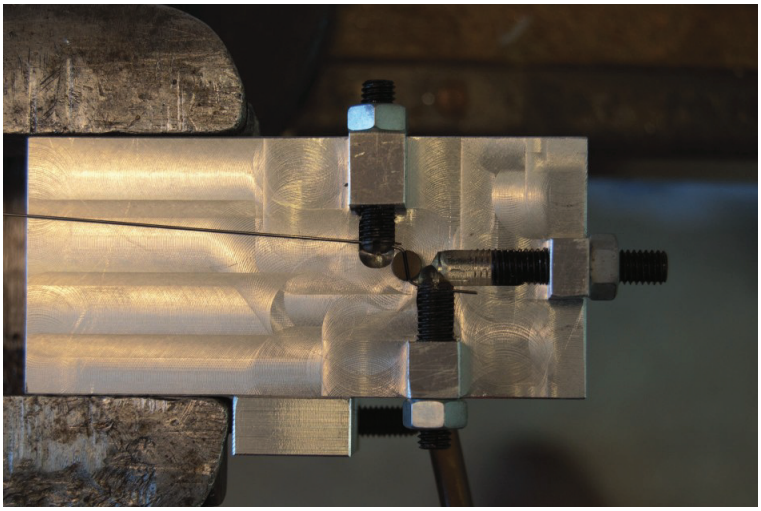

Figure 4.5: Prongs bending device used in the KTH laboratories in Stockholm (courtesy of Marco Ferro).

4.2.4 Wire soldering

Platinum wire was selected for the hot-wire sensors. Althought its mechanical characteristics are not as good as tungsten, it is available in diameters smaller

than 5 μm, unlike tungsten wires. In the making of these probes, 1,24 μm and 2,56 μm diameter wires were used. These platinum wires are made with the Wollaston process and are coated with silver. To remove the silver, the portion of the wire that will be used is kept in the 65% nitric acid solution for approximately 15 minutes, this removes the silver coating without damaging the platinum core. It is better not to use the same acid solution that was previously used for prongs etching, as it now contains a lot of material and impurities that can damage or contaminate the wire. The platinum wire is attached to the steel prongs via *soft-soldering*: it is a process in which two metal pieces are joined together by melting and flowing a filler metal, called *solder*, into the joint without melting the workpieces. As solder material, a regular Sn60Pb40 tin-lead alloy with a 183°C melting point was used. The steel prongs have an oxide layer that doesn't allow regular water-based flux to be used. A more aggressive zinc chloride based flux is used to remove the oxide layer from the tip of the prongs. Now a description of the procedure used to solder the wire will be given, while in figure 4.7 are schematically represented the main steps. A little amount of flux is deposited on the tips, with the help of a little brush or a cotton bud. The zinc chloride is mildly corrosive so it is better to put as little as possible and avoid contact with the part of the prongs that are not in the immediate vicinity of the wire (less than 1mm from the tip is enough). After this, some solder is put on the soldering iron's tip, it will melt and form a little bubble that sticks on the soldering iron. Then a uniform solder layer has to be deposited on the prongs' tip. This is done by moving the soldering iron close to the prongs until they are immersed in the melted solder bubble (only the portion previously wetted with the flux). When the iron is moved away, a layer of solidifying solder will be left on the tips (figure 4.7a). Before starting with the wire positioning, another very little amount of flux can be put on the prongs, this will help keep the wire in place through surface tension, until the soldering process is completed. The soldering has to be carried out with the microscope. Furthermore, micromanipulators are used to position the wire in place and to move the soldering iron in contact with the prongs. For this thesis a regular soldering iron was used, with the addition of an adapter to mount it on a micromanipulator (see figure 4.6). With the probe fixed under the microscope the uncovered portion of the wire is placed across the prongs using one micromanipulator, as close to the tips as possible and in horizontal position. This can be done easily by making contact first with the prong further away from the wire (on the right side in figure 4.7b) then sliding the wire towards

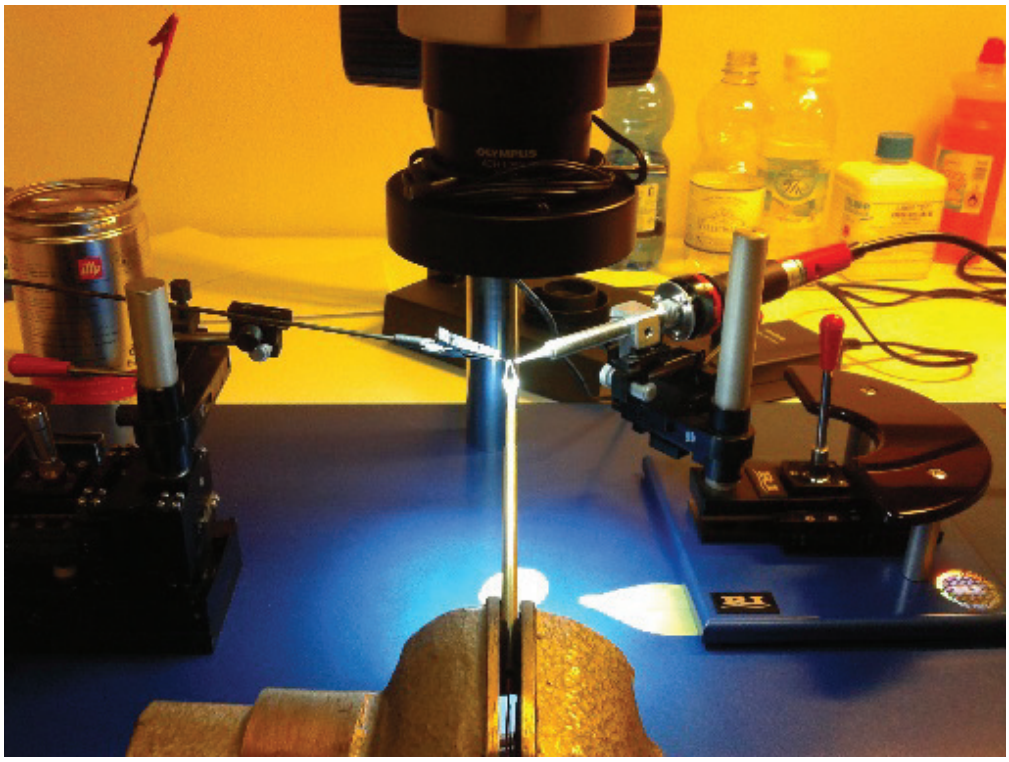

Figure 4.6: The hot-wire manufacturing station. On the right is visible the micromanipulator with the soldering iron, on the left the one used to move the wire. At the centre, the probe is placed under the microscope and fixed in a vise.

the other prong and lowering it until it touches the second prong and the loose end of the wire hanging off the far-side prong is not excessive, as this part will have to be removed at the end and will therefore be "lost". After it has been visually verified that the wire is in contact with both prongs with a satisfactory position and orientation, the wire micromanipulator is left in the same position and soldering can take place. The manipulator with the soldering iron is used to put it in contact with the prongs, one at a time. First the prong with the loose end of the wire (figure 4.7c), so that if during the procedure the wire is moved, it can still be re-adjusted. When the soldering iron is put in contact with the prongs, care must be taken to avoid any excessive displacement of the prongs' position. It is possible to see with the microscope when the solder becomes liquid (when this happens it changes rapidly to a more shiny and darker texture) and covers the part of the wire in contact with the prongs. As soon as this happens, the soldering iron can be moved away from the prong. If no effect is visible, the soldering iron temperature might be too low, or the tip of the

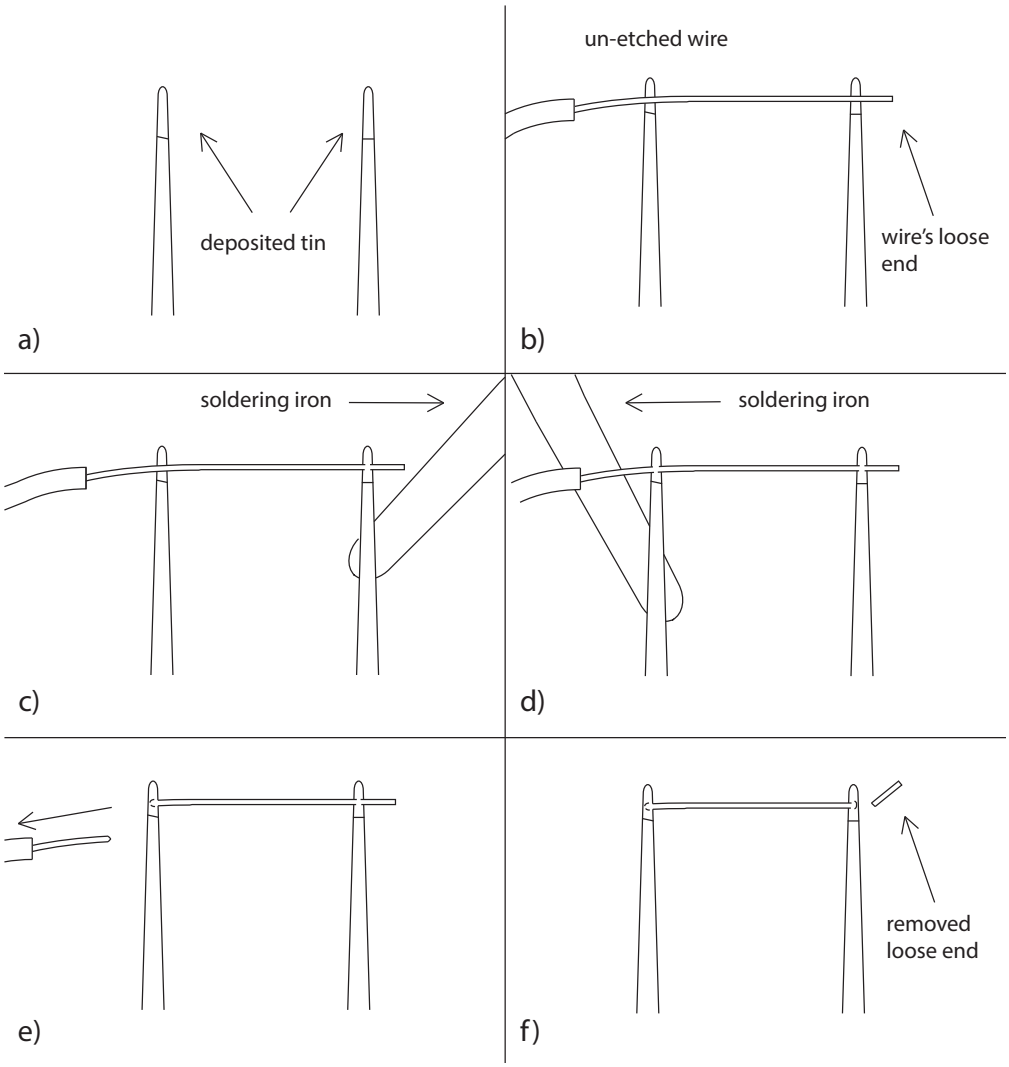

Figure 4.7: A simplified visual representation of the wire-soldering phase: a) tin deposition, b) wire placing, c) right prong soldering, d) left prong soldering, e) wire separation, f) wire's excess removal.

soldering iron might not be clean. After the operation is carried out for both prongs, a multimeter attached to the probe's electrical connections is used for resistance measurement. When the resistance reading approaches the expected value (known from the material resistivity and the prongs spacing) it means that the soldering was succesful. If an open circuit or a resistance in the range of kΩ or MΩ is returned as result, the soldering was unsuccesful or incomplete and must be done again. To complete the sensor, the unetched part of the wire attached to the manipulator is moved away until it separates from the etched part soldered on the prongs (figure 4.7e). Depending on where the wire breaks,

a portion of etched wire hanging from the left prong might have to be removed. This has to be done by hand and with extreme care, in order to avoid breaking the newly soldered wire (figure 4.7f). A cotton bud or piece of thread (even a hair) can be used for this purpose. In figure 4.8 is shown a close up of a finished sensor, while in figure 4.9 three probes with different spacing are compared.

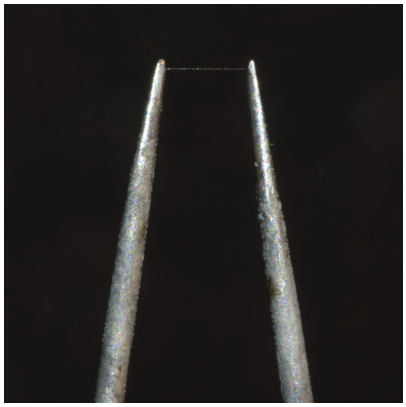

Figure 4.8: A close up photo of a hot-wire, showing the wire and the final part of the prongs (courtesy of Marco Ferro)

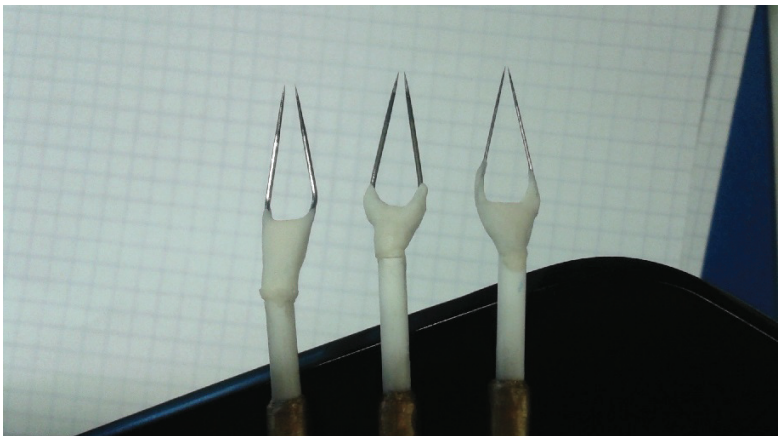

Figure 4.9: Three single wire probe with different spacing, from right to left: 1 millimiter, 500 microns and 250 microns.

Chapter 5

Experimental results

5.1 Coaxial Aerodynamic Tunnel facility

The facility used for the experiments is the *Coaxial Aerodynamic Tunnel* (CAT) of the university of Bologna, located in Forlì. The CAT was designed by Buresti at the aerospace engineering department of the university of Pisa. The facility can be used for mixing layer studies as it consists of two coaxial jets; for this experiment however, as the main aim is the study of resolution effects in a turbulent jet flow, only the inner jet was used. The facility schematics is shown in figure 5.1. The CAT is composed of two indipendent centrifugal fans driven by two three-phase induction motors that are controlled in frequency, either manually or trough Labview VIs. Two pre-settling chambers are placed downstream each fan to reduce the disturbances and pressure fluctuations. Four plastic hoses connect the outer jet pre-chamber to the corresponding settling chamber to increase the symmetry of the flow, while a simple diverging pipe connects the inner one. Flow conditioning is performed by means of three screens and a honeycomb in the inner pipe as well as five screens and a honeycomb on the outer circuit. The inner and outer contraction ratios are 11:1 and 16.5:1, respectively, whereas the inner and outer coaxial nozzles, of exit diameter D_i=50mm and D_o=100mm, end with two straight pipes of constant section of 100 mm length. The experimental facility is placed in a large laboratory (a hangar) and the exit of the coaxial jet is far enough from surrounding walls and the floor, ensuring that the experimental conditions resemble that of a jet in an infinite environment. The traversing system is composed of two slides driven by stepper motors that allow probe movements in the axial and radial directions. The system is fully automatic and is controlled via digital input by a desktop PC. A Dantec Streamline 90N10 Frame in conjunction with 90C10 CTA modules were used

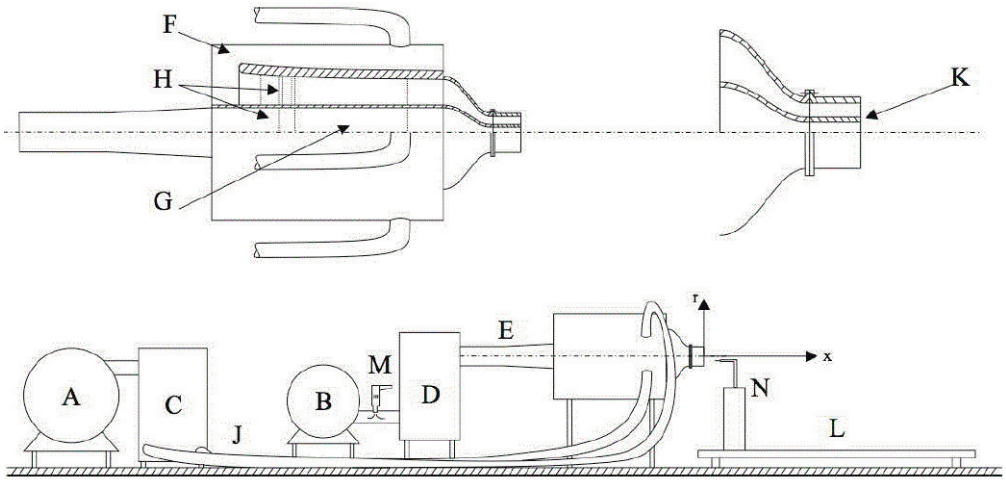

Figure 5.1: Schematic of the Coaxial Air Tunnel (CAT) facility: A) outer jet blower, B)inner jet blower, C) outer jet pre-settling chamber, D) inner jet pre-settling chamber, E) inner jet diffuser, F) outer jet settling chamber, G) inner jet settling chamber, H) screens and honeycombs, J) outer jet hoses, K) close-up of the jet exit with the thick separating wall, L) axial traversing, M) heat gun, and N) radial traversing.

Figure 5.2: CAT facility

for hot-wire measurements, while a NI BNC 2120 was the connector block and the acquisition card was a NI PCI 6221. The different type of sensors used are reported in table 5.1

Sensor	Material	length	diameter	l/d	α
home-made probe 1	Platinum	$250\mu m$	$1,27\mu m$	≈ 200	$3.93 * 10^{-}3$
home-made probe 2	Platinum	$500\mu m$	$2,54\mu m$	≈ 200	$3.93 * 10^{-}3$
Dantec 55P11	Tungsten	$1200\mu m$	$5\mu m$	≈ 240	$3.60 * 10^{-}3$

Table 5.1: Hot-wire sensors used for jet experiments.

Before carrying out the actual measurements, a series of preliminary operations were undertaken, in order to locate the jet axis and decide the acquisition time and frequency.

5.2 Jet alignament

Before acquiring any velocity measurements, the traversing system described in the previous chapter was aligned with the jet axis. This procedure was carried out by aligning first the traversing system with the geometrical axis of the jet, then by finding the real physical axis of the jet (which might not coincide with the geometrical axis) by taking velocity profiles at different distances.

5.2.1 Geometrical axis

In order to find the geometrical axis of the jet and to align the longitudinal slide of the traversing system with it, a cheap laser pen was used. Since the coaxiality of the laser source with the pen body is not guaranteed, a special holder for the pen was built (figure 5.3), that allows to sligthly move and rotate the laser pen with two sets of three screws that hold the pen at its ends. In this way it was possible to regulate the position and inclination of the laser pen until the laser is coaxial with the holder. For reference, the axis of a leathe machine was used. The holder was mounted on the machine, with the pen inserted, the screws were then adjusted until the laser corresponded with the leathe machine axis. To our surprise the laser source was found to have a deviation of more that 20 degrees with respect to the pen body. The holder was then mounted on the jet with a pvc adapter that fit tightly in the jet's exit, not allowing any movement. A paper target was taped on the traversing system's probe holder and the probe was moved back and forth, observing the laser spot movements

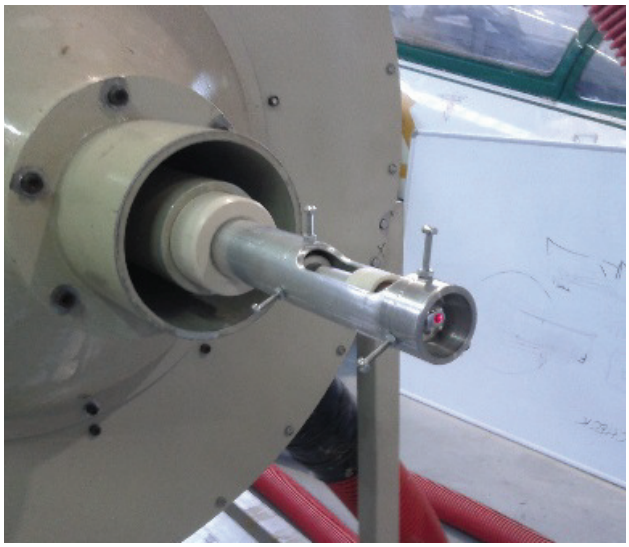

Figure 5.3: Device for jet-traversing alignament.

on the target. The traversing system was moved and inclined until the laser remained always on the target. The traversing system was aligned in this way up to 40 diameters from the jet axis.

5.2.2 Physical axis

The real axis of the jet might not coincide with its geometrical axis, due to the influence that the sorroundings may have on the jet itself. To verify the real position of the jet axis, after the geometrical alignament, longitudinal mean velocity profiles were acquired with a commercial hot-wire sensor with a length of 1mm and a diameter of 5μm. Profiles were taken at 10, 15 and 20 diametres fron the jet nozzle, with an exit velocity of 18 m/s. The axis position was located individually for each profile by fitting the data with a fourth order polynomial, then computing the maximum (figure 5.4). From the so obtained axis coordinates, a linear fit was applied (figure 5.5). The result of this fit is considered to be the "real" axis position. It is important to point out that given the directions in which the probe can traverse, this procedure is able to detect the position of the axis on a vertical plane, but as far its position on an horizontal plane (parallel with the floor) is concerned, the result of the geometrical alignment is assumed to be correct.

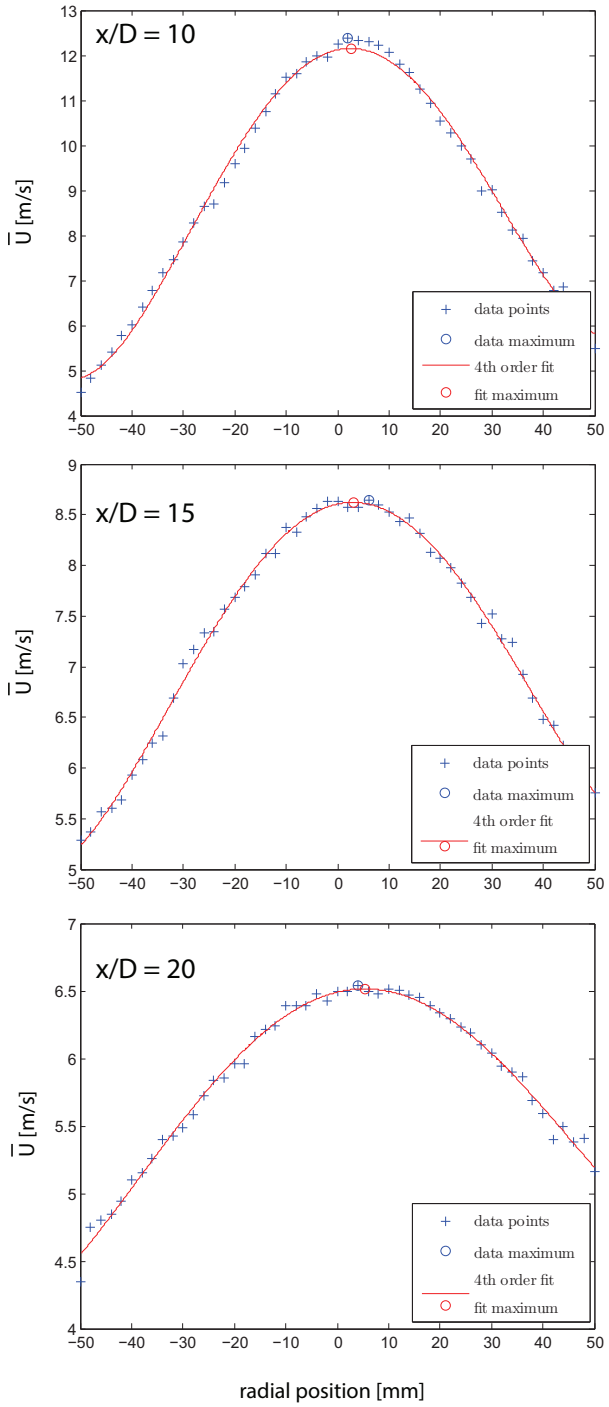

Figure 5.4: Mean velocity profiles and fourth order polynomial fit used to find their centers.

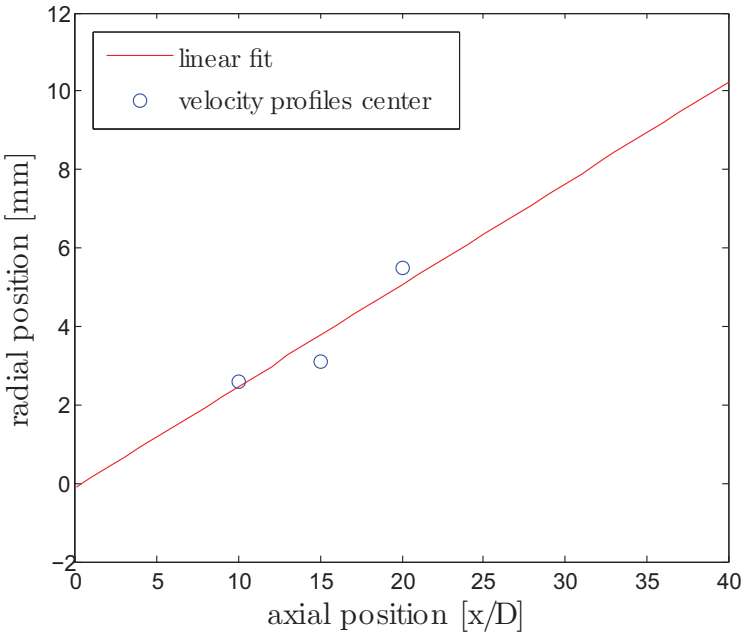

Figure 5.5: Profiles' maximum radial position, and axis position obtained by linear fit

5.3 Frequency analysis

To decide the sampling frequency to use and the low pass filter settings, a frequency characterisation of the jet velocity fluctuations was carried out. This operation has the aim to First Velocity measurements were taken at the centerline, at 10, 20, and 30 diameters from the jet exit with a sampling frequency of 40kHz and a total acquisition time of five seconds. The Power spectral densities were computed with Bartlett's method (non-overlapping segment with a rectangular window) and are shown in figure 5.6. From theory (see equation 2.37) we know that the integral of the PSD obtained from a serie of velocity measurements is equal to the variance of said time serie. To "see" how much variance (i.e. turbulence intensity) we filter by using a lower acquisition frequency we can compute the value of the PSD integral obtained using different upper integration limits, of course the higher the frequency we consider, the higher the integral value (see figure 5.7). In this case the PSD wasn't computed using Bartlett's method but instead all the data was used in a single FFT, as otherwise the windowing would lead to an error and the integral wouldn't be the signal's variance. As expected, the measurements at 10 D show that near the jet exit the fluctuations of the signal are at higher frequencies when com-

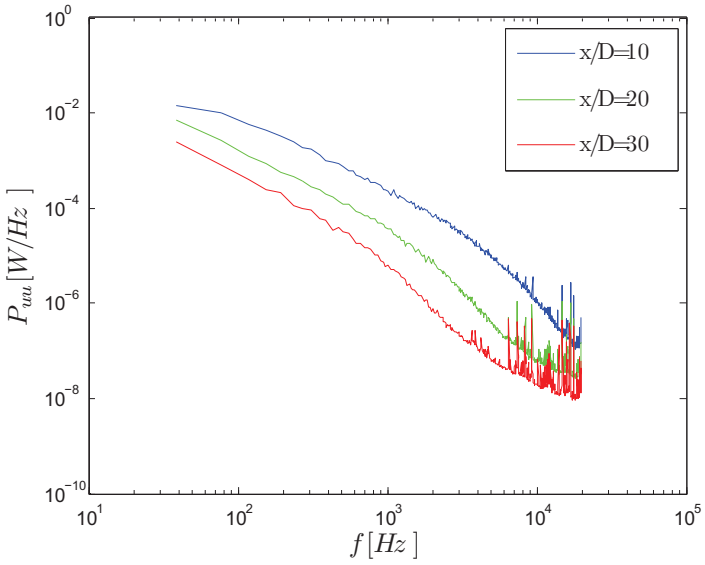

Figure 5.6: PSDs obtained with Bartlett's method at different axial position along the centerline, from velocity time series acquired at 40 kHz.

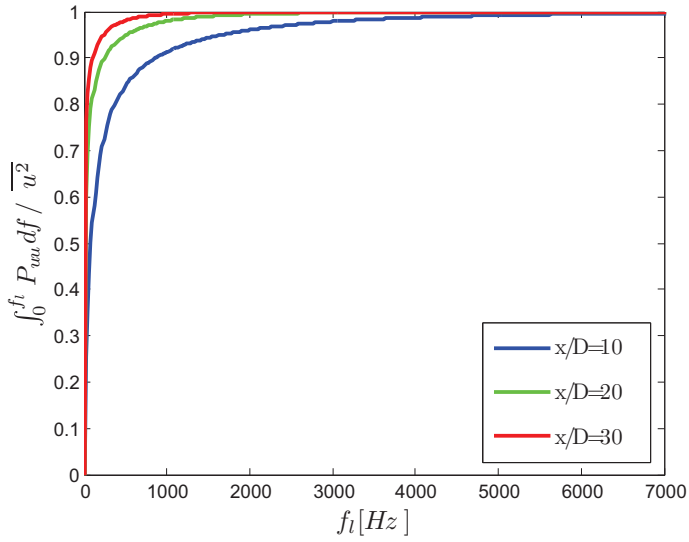

Figure 5.7: Power spectral density integral, normalized with the variance, as a function of the upper integration limit f_l

pared with the two other positions, hence a higher frequency is required in this case to reach the same integral value. From this results it was decided that velocity fluctuations up to 5 kHz had to be measured, therefore, as stated by the Nyquist theorem, a sampling frequency of 10kHz was employed.

5.4 HW calibration

Calibration of every hot-wire sensor was carried out before each set of measures. The flow at the jet exit was used for calibration, and as a reference velocity sensor a prandtl tube was used. During calibration (as well as during subsequent measures) temperature was acquired by means of a K type termocouple placed on the probe holder. In this way it was observed that during calibration at the jet nozzle, the flow is gradually heated as velocity is increased, with a difference of $\approx 1.5°C$ between the lowest and highest velocity points. To compensate the effect of temperature variation, the calibration's reference temperature T_{ref} was taken as the average temperature of the calibration points, then the voltage values obtained were corrected using the temperature compensation expression:

$$E(T_{ref})^2 = E(T_c)^2\left(1 - \frac{T_c - T_{ref}}{a_w/\alpha}\right)^{-1} \tag{5.1}$$

Where T_ref is the average calibration temperature, and T_c is the single calibration point's temperature acquired with the termocouple. After the anemometer signals were corrected in this way, a calibration curve was fitted on the points, the particular expression used is a fourth order polynomial:

$$U = C_0 + C_1E + C_2E^2 + C_3U^3 + C_4U^4 \tag{5.2}$$

the five calibration constants appearing in the expression were calculated using a least squares fitting method. In figure 5.9 are shown the calibration curves for the corrected and uncorrected hot-wire signal. As can be seen, the temperature correction as a very little influence on calibration as the temperature drift experienced is relatively small. The effect is more noticeable at high velocities, because the jet flow slightly increases its temperature. This temperature drift effect can be partially eliminated by turning on the CAT facility and letting it run for $\approx$ 20 minutes before carrying out the calibration.

Figure 5.8: Hot-wire sensor and Prandtl tube at the jet nozzle during calibration.

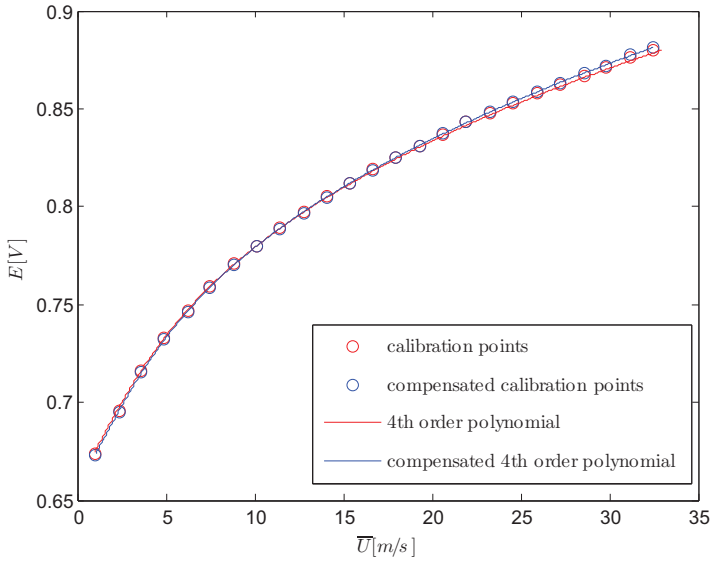

Figure 5.9: Calibration points and curves before and after temperature compensation

5.5 Preliminary axial measurements

A set measurements were taken on the jet centreline from the exit up to nearly forty diameters. This measures had the aim to check the response of the in-house constructed probe with the commercial one, but also to make a first carachterization of the flow field and possibly identify some areas of interest to further analyze with successive measurements in search for a possible spatial resolution effect. The jet exit velocity was approximately 19,5 m/s, corresponding to a Reynolds number based on the diameter of $Re_D = 62181$. The measures were acquired at 10KHz, acquisition times were as follows: 12,5 seconds for points within the first ten diameters, 25 seconds for the points between 10D and 20D, 50 seconds for points between 20 and 30 D, 100 seconds for points beyond 30 diameters from the exit. In figure 5.10 are shown the mean axial velocity results, where a good agreement between the sensor can be observed. Up to 5 diametrs from the exit the potential core is visible, and a mean velocity approximately equal to the jet's exit velocity can be observed, then the mean velocity starts decaying at first at a higher rate, then this decay-rate reaches a constant value around 20-25 diameters (self-similar region). The variance of the axial velocity, reported in figure 5.11 starts at zero, then exhibits a peak at 9-10 diameters from the exit and gradually decays towards zero as we move downstream. The skewness and flatness factors present respectively a positive and negative peak at 5-6 diameters (where the potential region ends), then rapidly returns to the canonical values of a Gaussian PDF, i.e. 0 for the skewness and 3 for the flatness. The negative skewness zone at the end of the potential core indicates an asymmetrical PDF and is caused by parts of turbulent flow of the shear layer entering the potential core. Based on these results, it was decided to further investigate the peak in the variance located approximately at x/D=10, where a possible spatial resolution effect would consist in the attenuation of the variance for the bigger sized sensors. From the previous data it does appear as if the smaller sensor detects a higher variance, but this single set of measurements in not enough to draw any conclusion. For what concerns the flatness and skewness factor, the points are too few in this measuraments to carachterize any behaviour and probably statistical convergence is also an issue.

5.5.1 A note on sensor drift

During the analysis of some of the data obtained during experiments, a strange behaviour of the mean velocity was observed for some of the sensors used. The

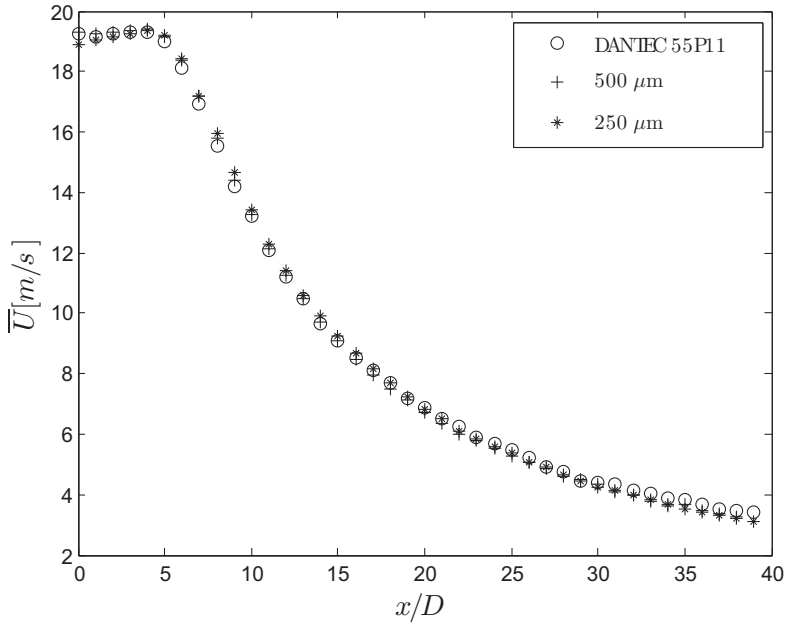

Figure 5.10: Mean axial velocity as a function of distance from the jet nozzle. $Re_D = 62181$.

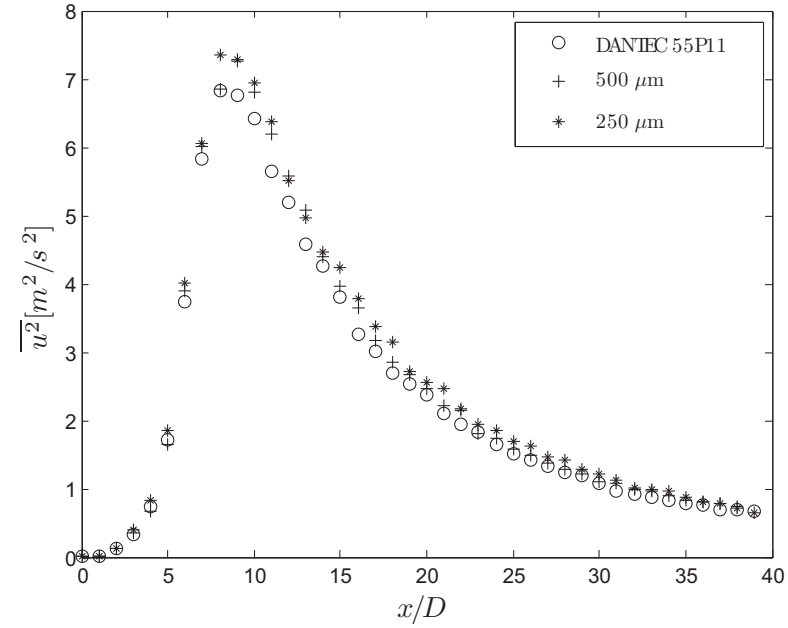

Figure 5.11: Axial velocity variance as a function of distance from the jet nozzle. $Re_D = 62181$.

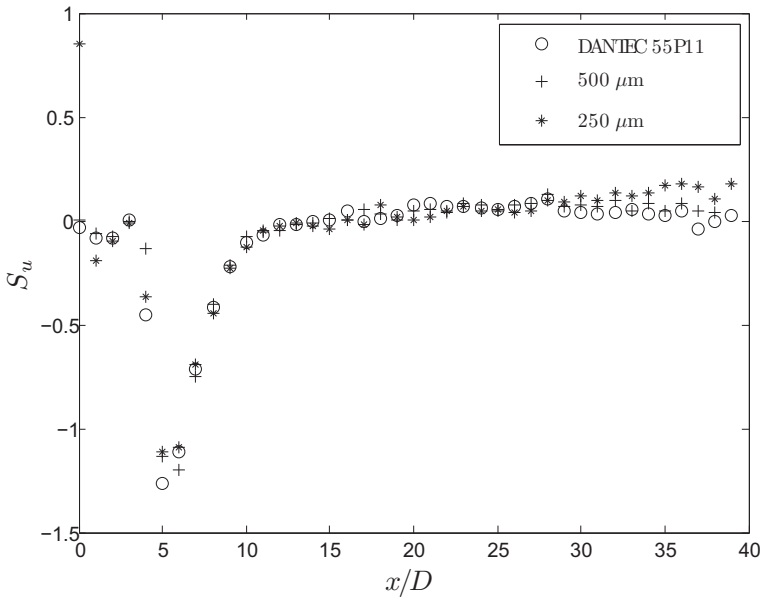

Figure 5.12: Axial velocity skewness factor as a function of distance from the jet nozzle. $Re_D = 62181$.

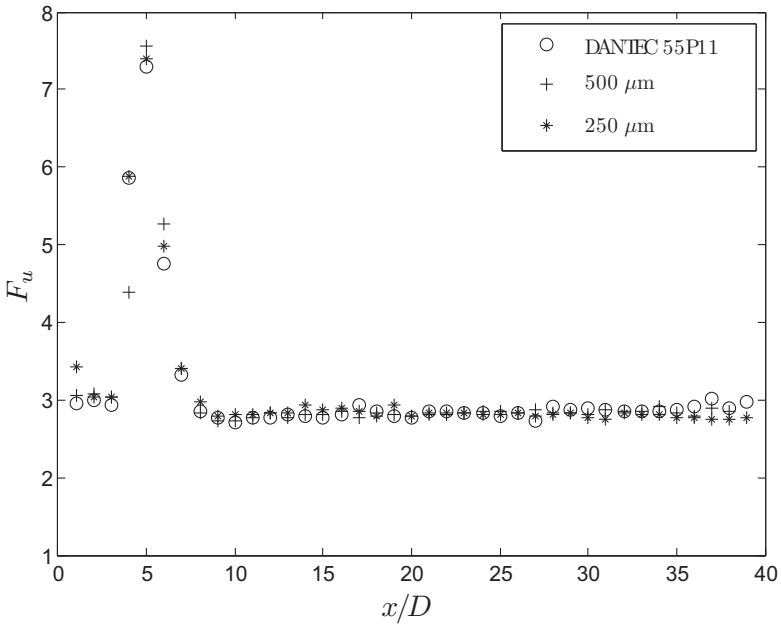

Figure 5.13: Axial velocity flatness factor as a function of distance from the jet nozzle. $Re_D = 62181$.

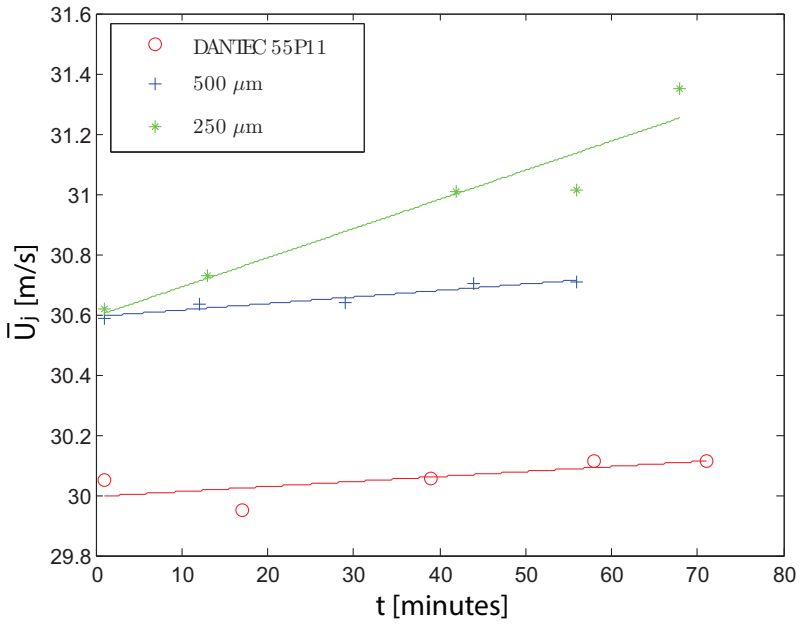

Figure 5.14: Jet exit velocity as a function of time measured with three different sensors. In this case the $250\mu m$ sensor experiences a drift.

deviation in the mean velocity measured by different sensors for the same fan setting is of such a magnitude ($\approx$ 1-2 m/s) that it cannot be explained simply with a difference in the fan output given by a change in ambient conditions. An example of this behaviour is shown in figure 5.14, where the jet exit velocitywas acquired during periodically for three different sensors. Observing the data it is clear that while the red and blue sensors experience variations that could be explained with a real change in the jet exit velocity, the green one is clearly sensing a difference in velocity that can't be "real". In fact comparing the data of all the calibrations used, the difference in velocity sensed by the Prandtl tube was found to be $< 0.5m/s$ for a same frequency setting of the asyncronous motor. The conclusion is that some of the sensors used had a drift in their signal, probably caused by insufficient aging. This effect was partially compensated by a regular calibration of the hot wire, but is notheless present on the data, and prevents the mean velocity data of different sensors to agree exactly. Unfourtunately there wasn't the time to analyze this drift phenomenon and to repeat the experiments. It is important to note however, that the drift in mean velocity of $\approx 2m/s$ has none if very little effects on higher order statistics, particularly on velocity variance that is were the most interesting results were obtained.

5.6 Single point statistics

Taking into consideration the observations made at the end of the previous section, for the following set of measures it was decided to focus in the region between 4 and 12 diameters, increasing the number of measuring points and the acquisition time. It was decided to acquire data on the centerline, to avoid errors caused by temperature fluctuations. In fact if the jet flow temperature and ambient temperature are different, in the shear layer the ambient air that gets entrained in the jet causes the hot-wire to measure in a flow with fluctuating temperature, but the thermocouple is not able to measure this fast temperature fluctuations and we are therefore not able to compensate the hot-wire signal for it. By limiting the measurements locations on the centreline and relatively close to the nozzle ($x/D < 15$) we can make the assumption that the hot wire doesn't experience this kind of problem and we can use the mean flow temperature for the signal compensation. This time the measurement points where selected at a distance of 10mm one from the other, for a total of 41 points, acquisition time was increased to 2 minute per point. The measurements were taken for three different cases of Reynolds number: One corresponding to the same case as before, with $U_j \approx 19.3m/s$ and $Re_d \approx 6.2 * 10^4$, one intermediate case with $U_j \approx 25.8m/s$ and $Re_d \approx 8.2 * 10^4$ and the last case using the maximum exit velocity possible in the CAT facility, with $U_j \approx 32.3m/s$ and $Re_d \approx 10.3 * 10^4$. It is important to note that during acquisition, the jet's exit velocity might sligthly change due to changes in ambient conditions (mainly pressure), hence the real Reynolds number for the single measurements, even using the same setting for the centrifugal fan, can slightly deviate. First let's consider the behaviour of the variance, in figure 5.15 are reported the three Reynolds number cases for the three different sensors. For all the three cases we can observe that the variance measured by smaller sensor appears consistently higher, with the one measured by the 1.2mm Dantec probe being the most attenuated and the one measured with the 250 μm home-built probe the highest, as we would expect. In particular, the response of the sensor starts to diverge from $x/D \approx 7$ and this difference increases up to $x/D \approx 9$, a value from which the difference in measured variance keeps an almost constant value. One important observation to be made is that this increase in variance for smaller sensors is seemingly independent on the Reynolds number, in fact for all three Reynolds number number cases, the variance returned by the $250\mu m$ wire probe is ≈ 1.25 times higher than the result given by the commercial probe, while the $500\mu m$ wire probe is ≈ 1.05 times higher. In figure 5.16 is reported the ratio between the

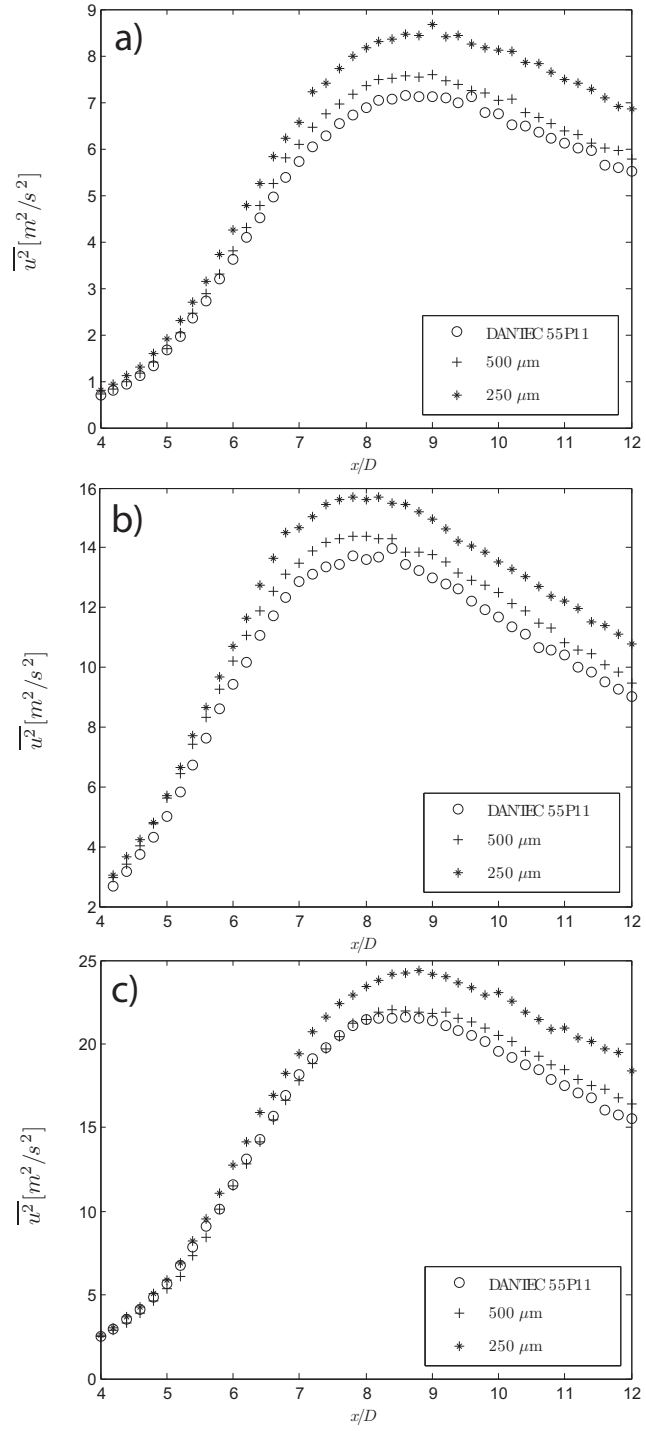

Figure 5.15: Axial velocity variance as a function of distance from the jet nozzle for different Reynolds number cases; a)$Re_D \approx 6.2 * 10^4$, b)$Re_D \approx 8.2 * 10^4$, c)$Re_D \approx 10.3 * 10^4$.

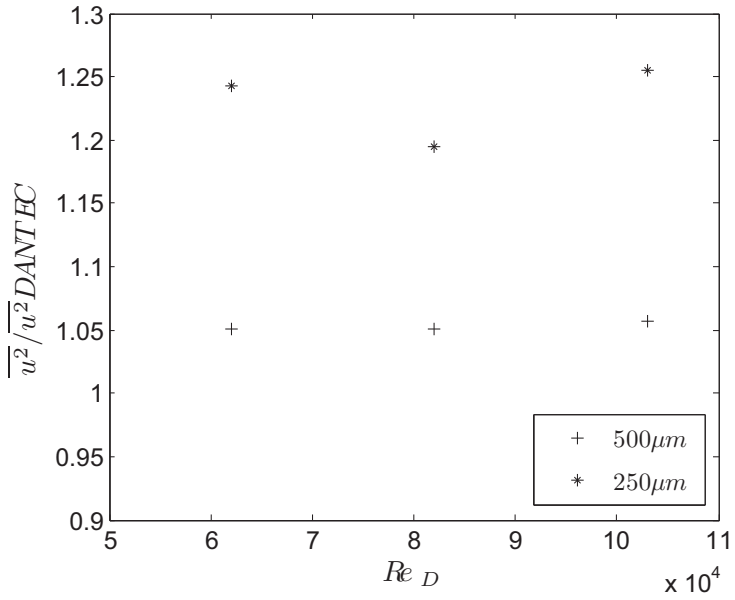

Figure 5.16: Variance ratio between the home-made probes and the commercial one, for $x/D = 12$.

variance of the home-made probes and the one of the Dantec probe, as a function of Reynolds number. From turbulence theory (in particular expression 2.4) we would have expected an increase in the filtering effect with increasing Reynolds number, while from the current measurement results this doesn't seem to be the case. On the other hand computing the skewness and flatness factor for this set of measurements doesn't return consistent results as for the second order moment case. The value of the skewness and flatness peak seems to vary slightly indipendently on the sensor used for the measurement or the Reynolds number considered. It was previously mentioned that there could be a drift in the actual jet velocity caused by a change in ambient conditions, so it is natural to speculate if the difference observed in the second order moment could in fact be caused simply by this phenomena: for example if between two set of measurements the jet velocity increased (increasing the Reynolds number), the second sensor would sense a higher variance, not thanks to a better spatial resolution, but only because the flow velocity had increased. To tackle this problem it was decided to make a final experiment utilizing a special probe with two parallel single wires of different dimensions, shown in figure 5.19. This special probe allows for simultaneous measurements with two different wires: one platinum wire with a diameter of 1.27 μm and a length of 250 μm and

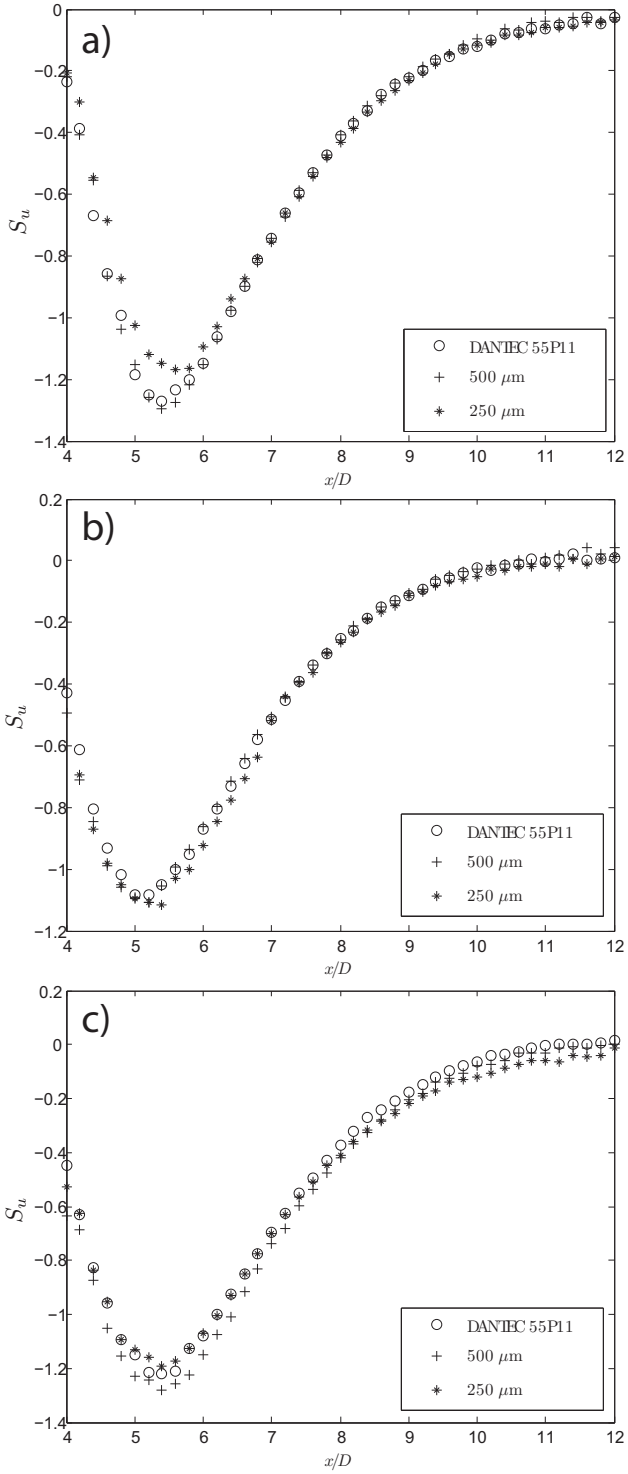

Figure 5.17: Axial velocity skewness factor as a function of distance from the jet nozzle for different Reynolds number cases; a)$Re_D \approx 6.2{*}10^4$, b)$Re_D \approx 8.2{*}10^4$, c)$Re_D \approx 10.3 * 10^4$.

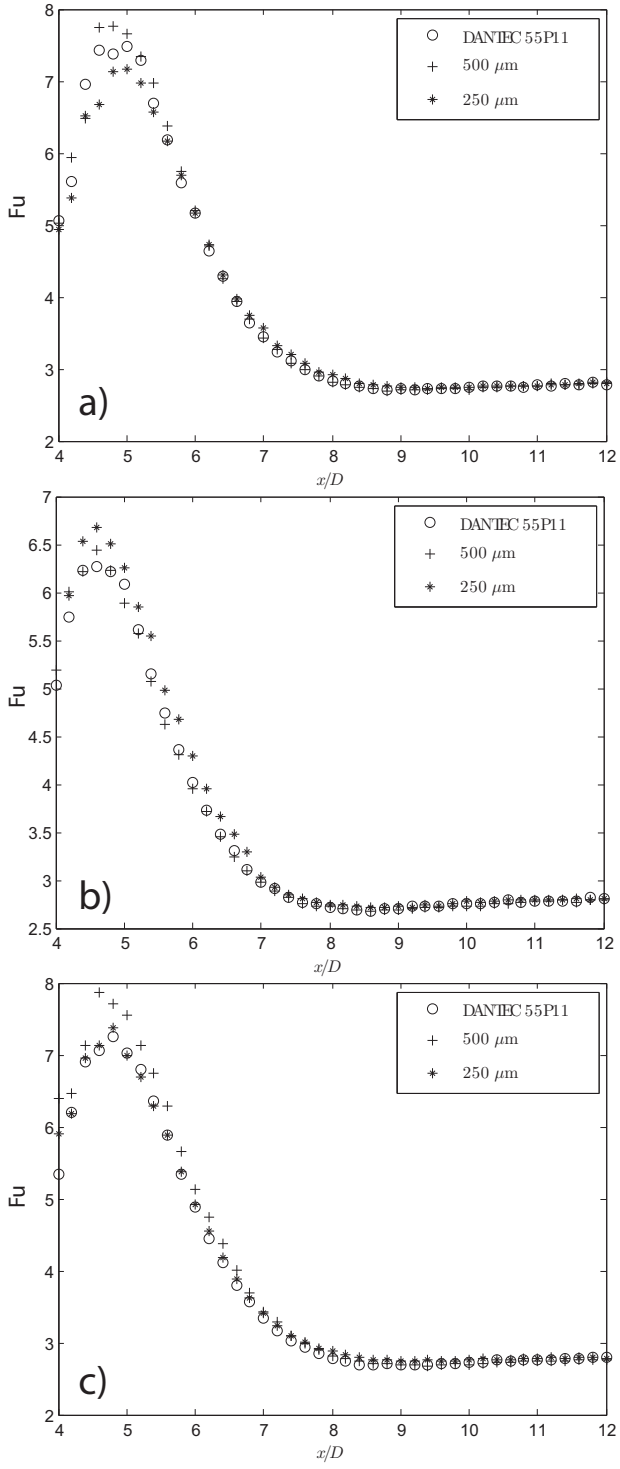

Figure 5.18: Axial velocity flatness factor as a function of distance from the jet nozzle for different Reynolds number cases; a)$Re_D \approx 6.2{*}10^4$, b)$Re_D \approx 8.2{*}10^4$, c)$Re_D \approx 10.3 * 10^4$.

Figure 5.19: Special probe with two parallel wire of different dimensions normal to the flow.

the other with a diameter of 2.54 μm and a length of 500 μm, corresponding to sensor number 2 and 3 of table 5.1. In this way it is certain that the two sensor will measure in the exact same conditions, overcoming the uncertainties associated with varying jet velocity, external disturbances and uncorrect probe positioning (the two wires are separated by only $\approx 500\mu$ and we can make the assumption that they measure in the same point). In this case the calibration was carried out simultaneously for the two wire. Acquisition time was further increased to 200 seconds per point. The exit jet velocity was set $\approx 30 m/s$ corresponding to $Re_d \approx 9.5 * 10^4$. In figure 5.20 the variance confirmed the behaviour already observed in the previous set of experiments, with the curves corresponding to wires of different lengths starting to diverge from $x/D \approx 7$, and then reaching at $x/D \approx 9$ a difference between their values that remains constant, with the smaller sensor returnin a value ≈ 1.22 times bigger than the other. In figures 5.21 and 5.22 are reported the third and fourth order moments for the 2-wire probe. Unlike previous measurements, in this case the smaller sensor appears to sense slightly higher values for both the skewness and the flatness factors, but the difference remains very small.

5.6.1 Convergence proof

To prove that statistical convergence was reached for the previous set of measurements, a "sliding average" method was applied, computing higher order

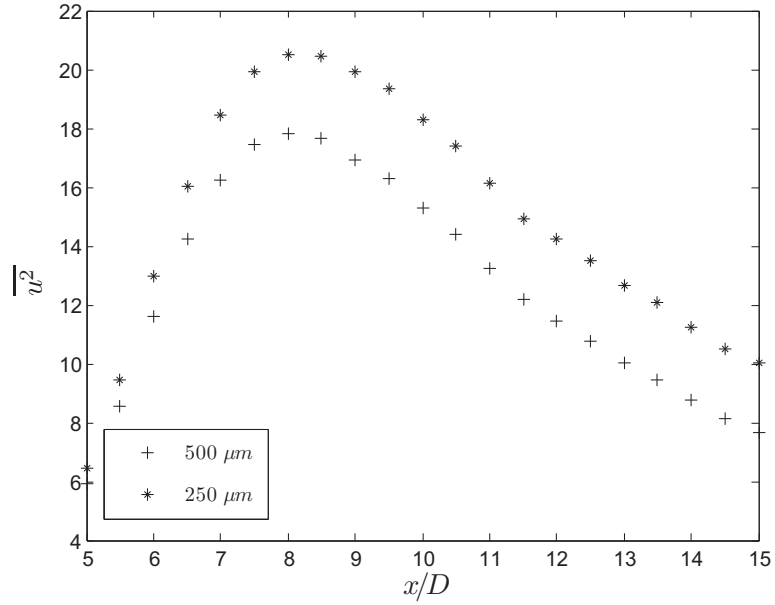

Figure 5.20: Axial velocity variance measured with the two wire probe. $Re_D \approx 9.5 * 10^4$.

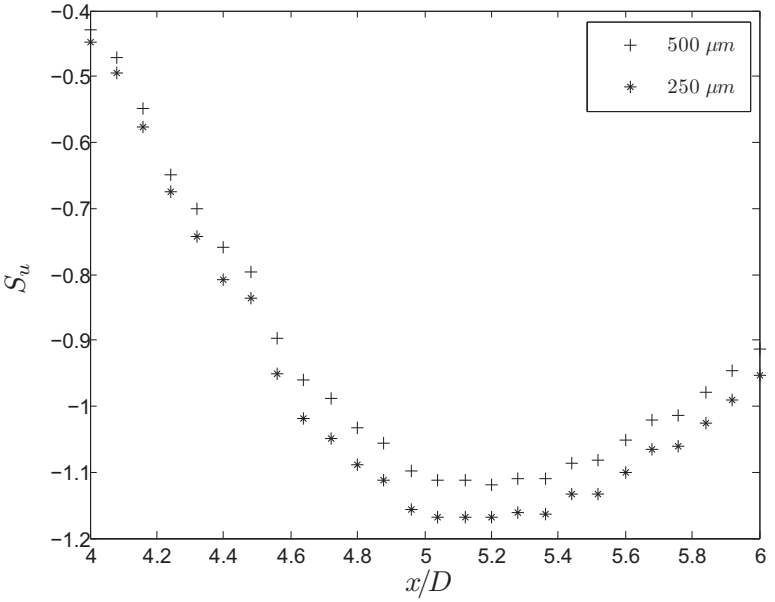

Figure 5.21: Axial velocity skewness factor measured with the two wire probe. $Re_D \approx 9.5 * 10^4$.

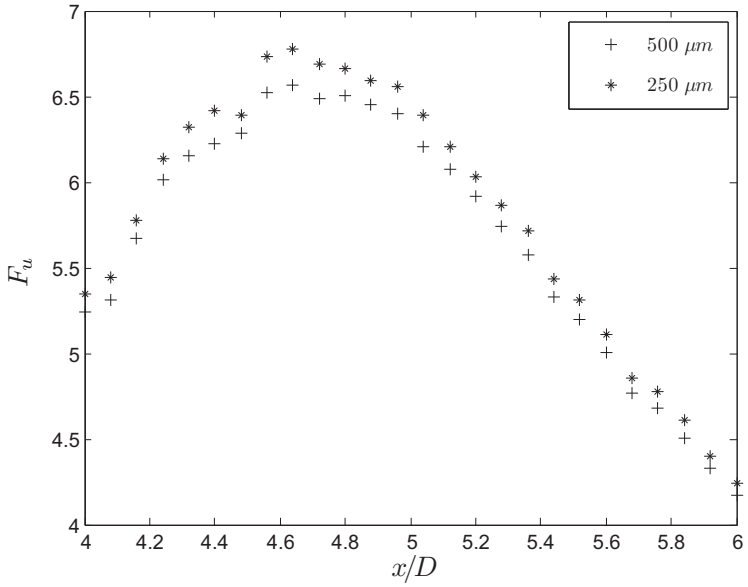

Figure 5.22: Axial velocity flatness factor measured with the two wire probe. $Re_D \approx 9.5 * 10^4$.

moments considering successively increasing portion of the data. If before all the points of the complete time serie are considered the statistics have reached a stable value, it means that statistical converegence has been reached. The results are shown in figure 5.23

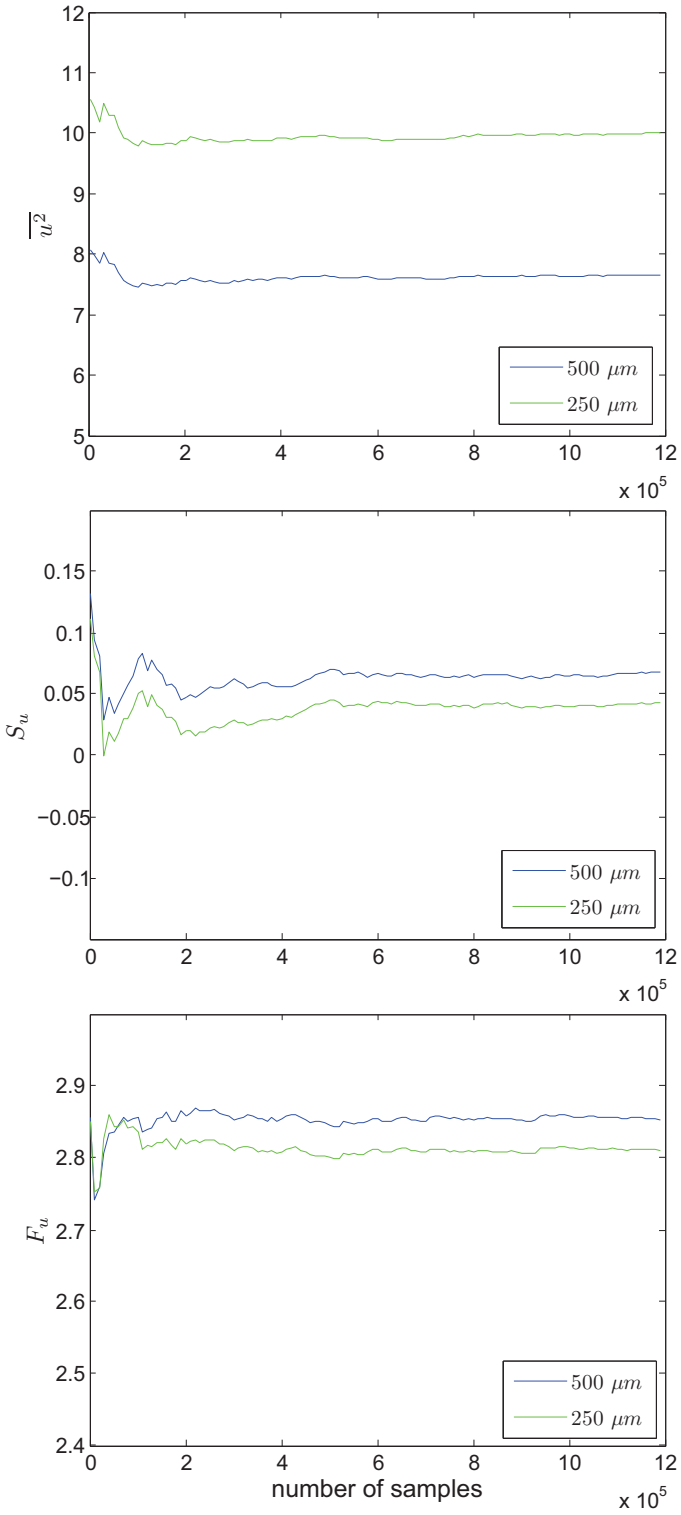

Figure 5.23: Statistics moments calculated for the data, as a function of the number of points considered, 2-wire probe case, $x/D = 15$, $Re = 10.2 * 10^4$.

5.6.2 Probability density function

Since a difference in the variance measured by the sensors was observed, also the PDFs must be different. Before computing the PDF, the mean velocity value was subtracted from the velocity time serie, in order to neglect the effect of the drift in mean velocity (the PDFs would appear slightly shifted on the x axis), in this way the fluctuations' PDF was obtained. In figure 5.24 are shown the fluctuation's PDFs given by the sensors on the two-wire probe. It can be seen that for fluctuations' values further away from zero, the PDF of the $250\mu m$ wire returns a slightly higher value, as can be expected from the higher variance value. This means that the smaller sensor detects more frequently the highest and lowest velocities, compared with the other one. This can be seen more clearly if we compute the integral of the PDF as a function of the upper integration limit, shown in figure 5.25. Looking at the first half of the curves, the integral of the $250\mu m$ PDF rises faster because the PDF itself has a higher value at its periphery compared with the other sensor's PDF. Finally in figure 5.26 are show in a three-dimensional plot the PDFs obtained for all the field of measurament, using the two-wire probe.

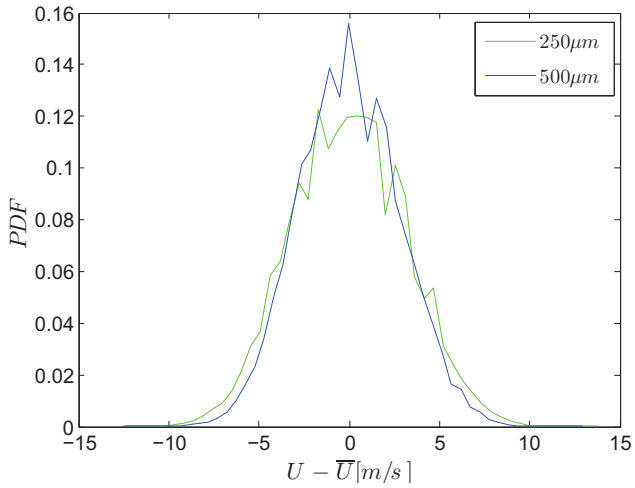

Figure 5.24: Velocity fluctuations PDF for the two-wire probe, $x/D = 15$, $Re = 10.2 * 10^4$.

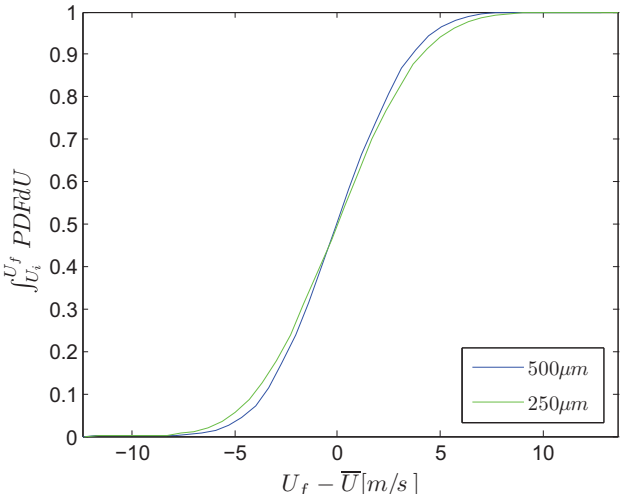

Figure 5.25: Integral of the PDF as a function of the upper integration limit U_f, $x/D = 15$, $Re = 10.2 * 10^4$.

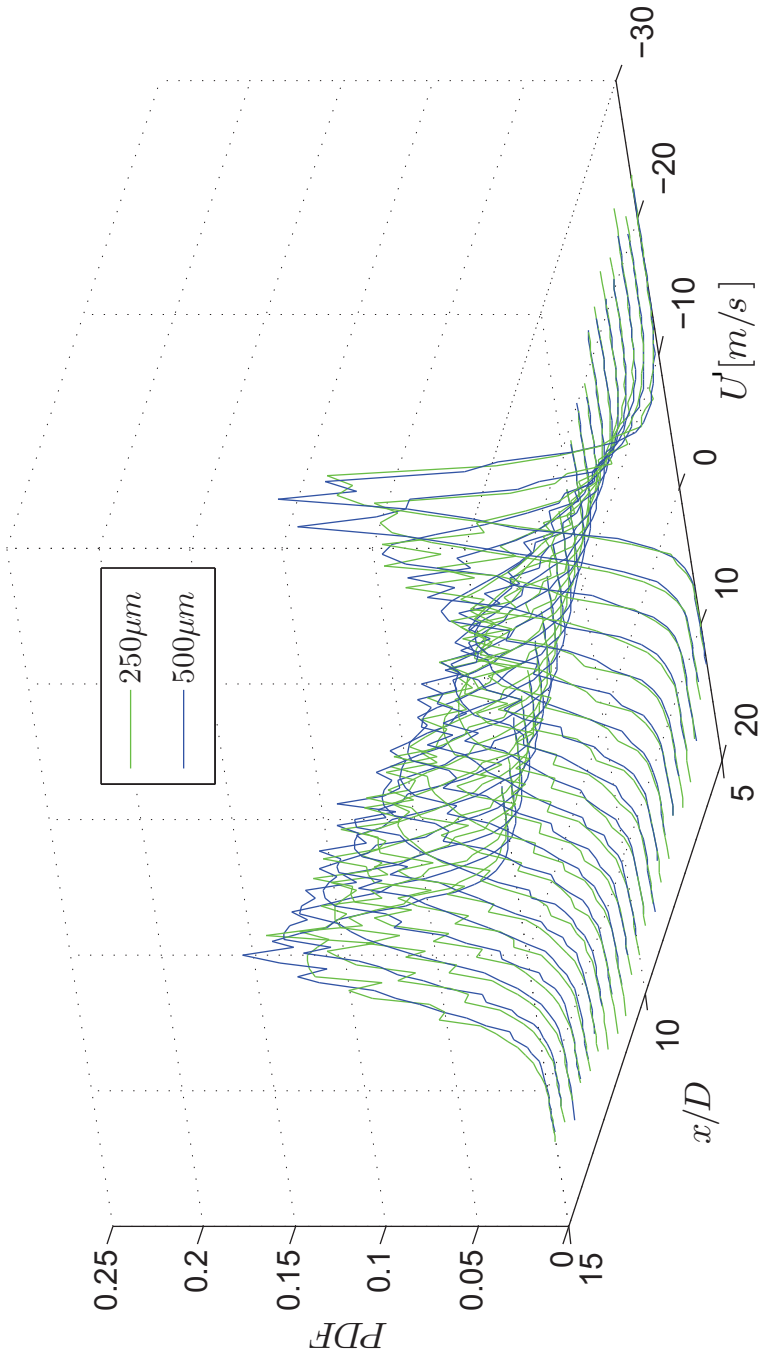

Figure 5.26: Velocity fluctuations PDF for the two-wire probe over all the range of measurements, $Re = 10.2 * 10^4$.

5.7 Power spectral density

From the axial set of measurements, power spectral densities were computed, using the Welch method illustrated in the theoretical background chapter (in this case with a Hanning windowing and a 50% overlap between data segments). In figure 5.27 is reported an example of the PSDs of the three sensor for the axial position $x/D = 9$, where the variance peak is located. The results shows that while at lower frequencies the spectra of the different sensors match nicely, at high frequency values, the smaller the sensor, the higher the PSD value. This is even more noticeable in the pre-multiplied spectra, shown in figure 5.28. We can compute the ratio between the spectra measured by different sensors, as a function of frequency considered, in figure 5.29. Using the 1.2 mm Dantec probe as a reference we can see that from a starting value of 1, the ratio grows as the frequency increases, but the 250 μm sensor grows faster than the 500 μm one. In figure 5.30 and 5.30 the PSD and pre multiplied PSD for all the axial positions are shown in three-dimensional plots; as can be seen the behaviour observed in $x/D = 9$ for the three sensors is consistent with the other positions.

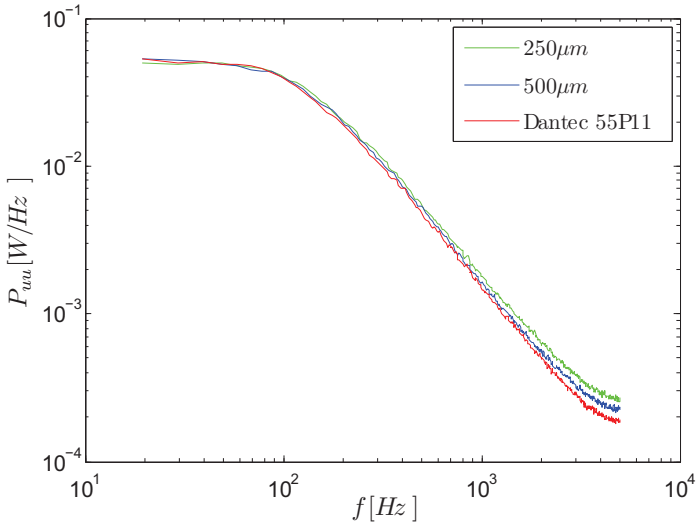

Figure 5.27: PSDs for different probe types at $x/D = 9$. $Re_D \approx 9.5 * 10^4$.

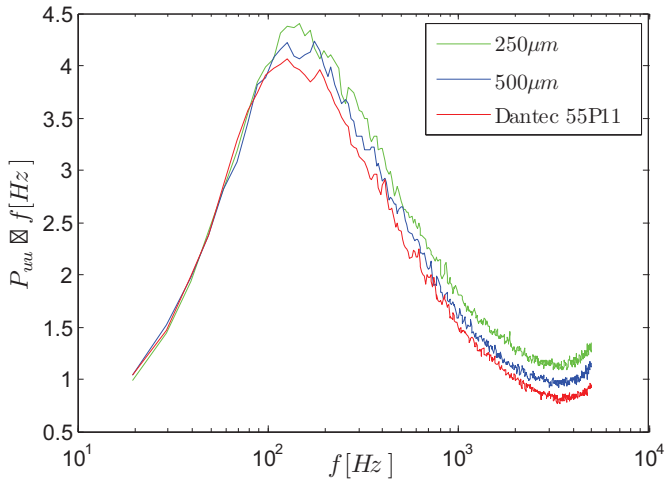

Figure 5.28: Pre-multiplied PSDs for different probe types at $x/D = 9$. $Re_D \approx 9.5 * 10^4$.

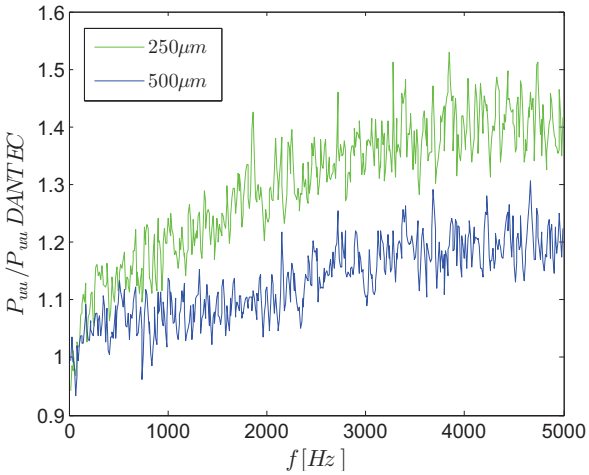

Figure 5.29: PSD measured by the two home-made sensor normalized by the PSD given by the Dantec probe.

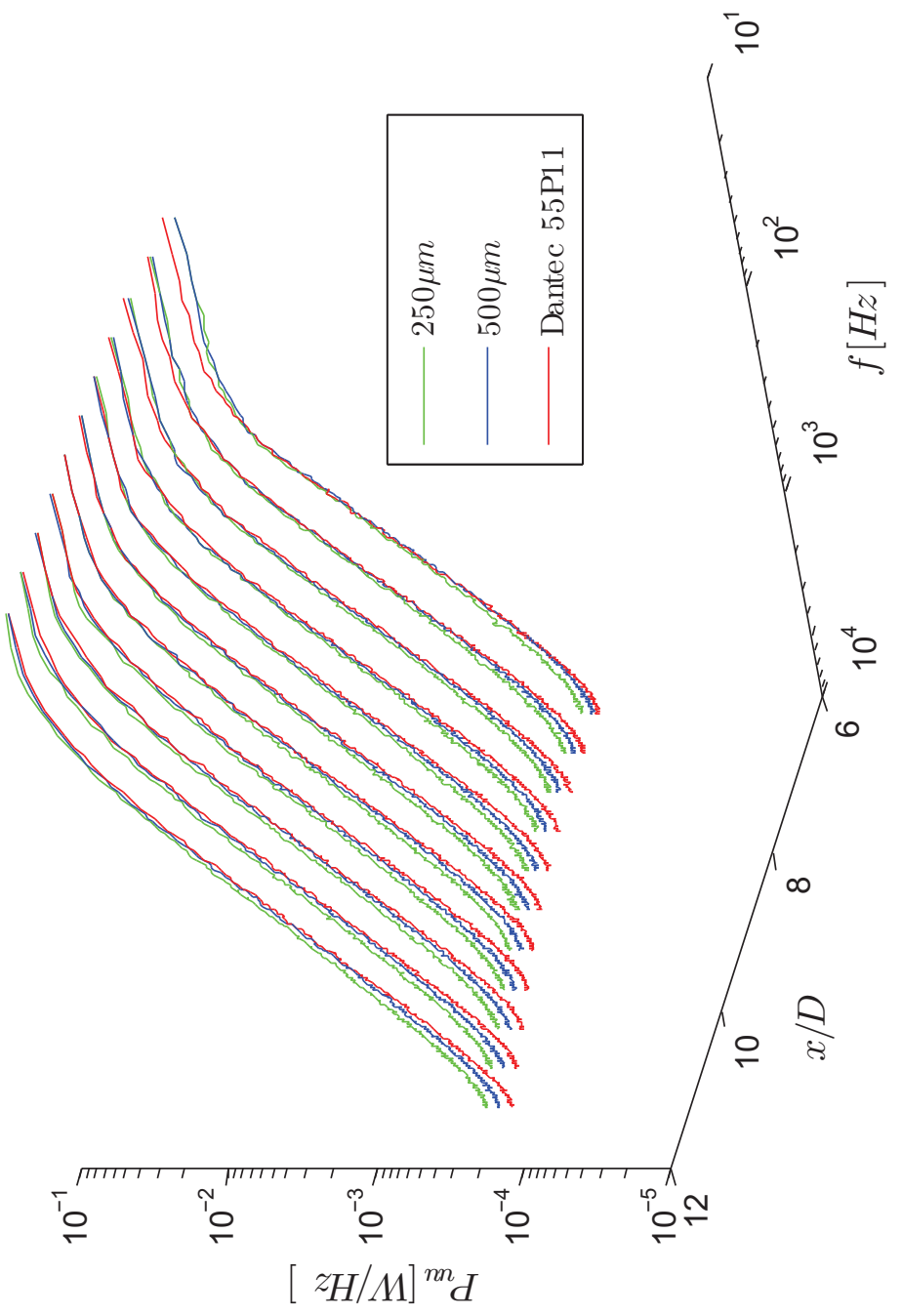

Figure 5.30: PSD measured by the three different sensors for all the axial positions. $Re_D \approx 9.5 * 10^4$.

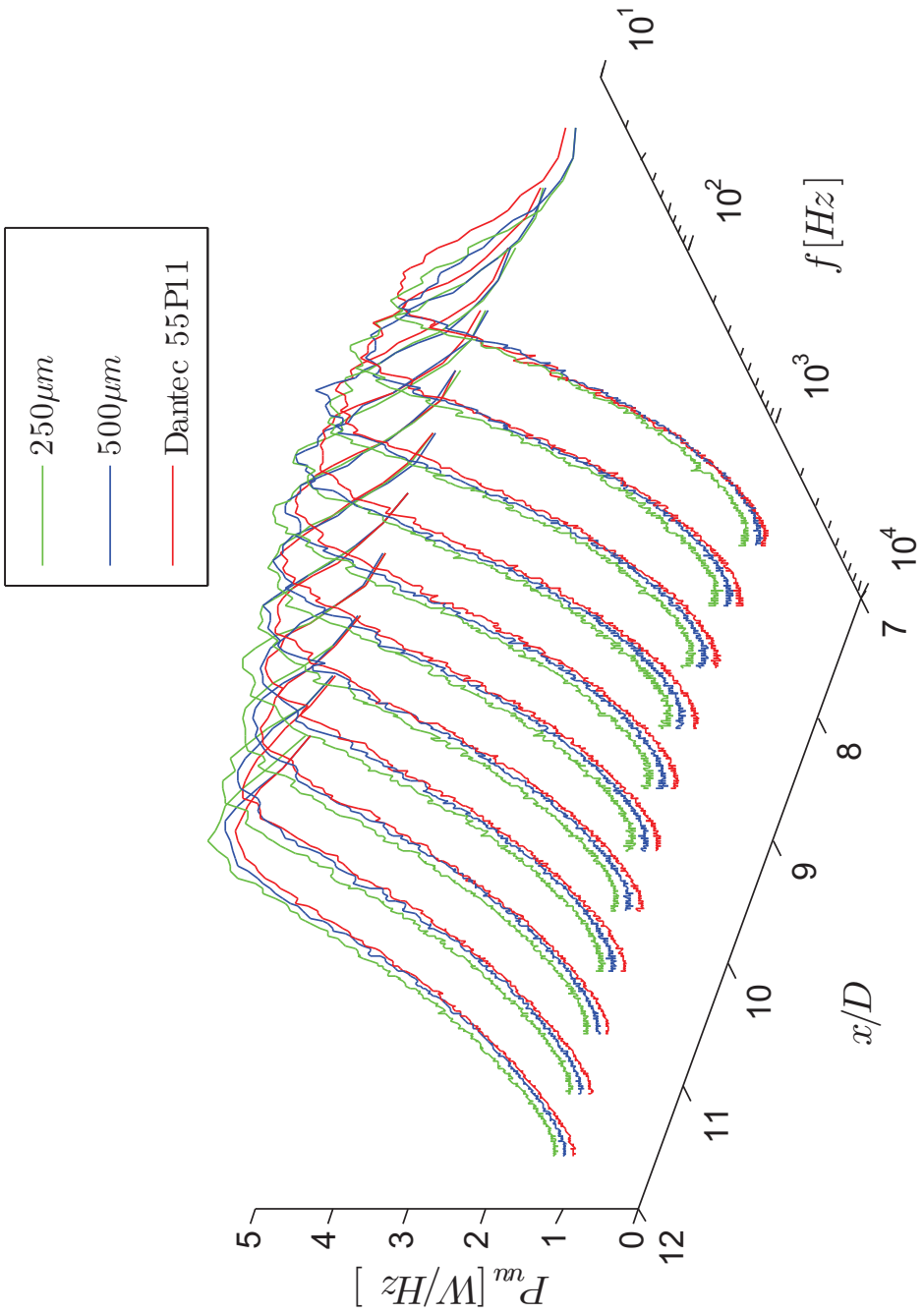

Figure 5.31: Pre-multiplied PSD measured by the three different sensors for all the axial positions. $Re_D \approx 9.5 * 10^4$.

Chapter 6

Conclusions

In this Master thesis, a working hot-wire laboratory was prepared, gathering the necessary equipment, learning and perfecting the techniques used for the manufacturing of these sensors. Home-made hot-wire sensors have the advantage of being relatively simple and cheap to make, and eliminate the time and cost connected with the repair. Furthermore, they can be produced in smaller physical dimensions compared to the commercial hot-wires, a feature that is of primary importance in high Reynolds number flows, were spatial resolution should be particularly high. The manufactured sensors were used to measure a turbulent jet with a diameter-based Reynolds number up to $\approx 10^5$. The data obtained with the small probes were compared to those obtained with a commercial hot-wire probe. In short the conclusions that can be drawn from the measurements campaign are as follows:

- The manufactured hot-wire sensors exhibits a good degree of agreement with the commercial probe, signaling their correct operation. Relatively speaking, they also show good durability, with only two wire breakages in over three weeks of measurements.

- From the measurements results in the turbulent jet, we found evidence that the 1.2mm commercial hot-wire probe introduces spatial filtering effects. While this was a known issue in wall bounded flows, this is a new and unexpected result for jets, as these flows are characterized by a lower energy-content at small scales. In particular we observed a consistent attenuation of the axial velocity along the jet centerline starting from $x/D > 7$.

- Spectral analysis shows that attenuation increases with increasing frequency, which supports the hypothesis of the probe behaving as a low-pass

filter with a cut-off frequency proportional to its length.

The result obtained also suggested what a future experimental campaign should focus on, to shed light on issues that couldn't be treated in a satisfactory way in the present work:

- No clear relation could be established between the observed filtering effect and the Reynolds number, to the contrary of what turbulence theory states. Further experiments covering a wider range of Reynolds number cases are needed for any conclusion to be made on this particular aspect.
- Although a small effect on the third and fourth order statistical moments' peaks located at $x/D \approx 5$ was observed with the two-wire probe, a more systematic study is needed.
- The experimental measures were concentrated in a relatively small area close to the jet nozzle. The development of the observed filtering effect beyond x/D = 15 is still to be investigated.

Bibliography

[1] J. D. Alamo and J. Jimenez. Estimation of turbulent convection velocities and corrections to taylor's approximation. *J. Fluid. Mech*, 2009.

[2] S. C. Bailey, M. Hultmark, J. Schumacher, V. Yakhot, and A. J. Smits. Measuraments of local dissipation scales in turbulent pipe flows. *Phys. Rev. Lett.*, 2009.

[3] H. H. Bruun. *Hot-wire anemometry - principles and signal analysis.* Oxford University Press, 1995.

[4] J. D. Cameron, S. C. Morris, S. Bailey, and J. Smits. Effects of hot-wire length on the measurement of turbulent spectra in anisotropic flows. *Meas. Sci. Technol.*, 2010.

[5] C. Chin, N. Nutchins, A. S. H. Ooi, and I. Marusic. Use of direct numerical simulation (dns) data to investigate spatial resolution issues in measurement of wall-bounded turbulence. *Meas. Sci. Technol.*, 2009.

[6] C. Chin, N. Nutchins, A. S. H. Ooi, and I. Marusic. Spatial resolution correction for hot-wire anemometry in wall turbulence. *Exp. Fluids*, 2011.

[7] G. Comte-Bellot, A. Strohl, and E. Alcaraz. On aerodynamic disturbances caused by single hot-wire probes. *J. Appl. Mech.*, 1971.

[8] M. Ferro. Experimental study on turbulent pipe flow. Master's thesis, KTH Mechanics, Stockholm, Sweden, 2012.

[9] M. Hultmark, A. Ashok, and A. J. Smits. A new criterion for end-conduction effects in hot-wire anemometry. *Meas. Sci. Technol.*, 2011.

[10] J. H. Hussein, S. P. Capp, and W. K. George. Velocity measurements in a high reynolds number, momentum conserving, axissymmetric turbulent jet. *J. Fluid. Mech*, 1994.

[11] N. Hutchins, T. B. Nickels, I. Marusic, and M. S. Chong. Hot-wire spatial resolution issues in wall-bounded turbulence. *J. Fluid. Mech*, 2009.

[12] F. E. Jorgensen. *How to measure turbulence with hot-wire anemometers - a pratical guide*. Dantec Dynamics, 2002.

[13] L. V. King. On the convection of heat from small cylinders in a stream of fuid: Determination of the convection constants of small platinum wires, with applications to hot-wire anemometry. *Proc. R. Soc.*, 1914.

[14] J. D. Li, B. J. McKeon, W. Jiang, J. F. Morrison, and J. Smits. The response of hot-wires in high reynolds numbers turbulent pipe flow. *Meas. Sci. Technol.*, 2004.

[15] P. M. Ligrani. Subminiature hot-wire sensor construction. Technical report, Naval postgraduate school, 1984.

[16] P. M. Ligrani and P. Bradshaw. Spatial resolution and measurement of turbulence in the viscous sublayer using subminiature hot-wire probes. *Exp. Fluids*, 1987.

[17] P. M. Ligrani and P. Bradshaw. Subminiature hot-wire sensors: development and use. *J. Phys. E.*, 1987.

[18] C. G. Lomas. *Fundamentals of Hot Wire Anemometry*. Cambridge University Press, 1985.

[19] I. Marusic, R. Mathis, and N. Hutchins. High reynolds number effects in wall turbulence. *Int. J. Heat Fluid Fl.*, 2010.

[20] I. Marusic, B. J. McKeon, P. A. Monkewitz, H. M. Nagib, A. J. Smits, and K. R. Sreenivasan. Wall-bounded turbulent flows at high reynolds numbers: Recent andvances and key issues. *Phys. Fluids*, 2010.

[21] R. Örlü. *Experimental studies in jet flows and zero pressure-gradient turbulent boundary layers*. PhD thesis, KTH Mechanics, Stockholm, Sweden, 2009.

[22] R. Örlü and P. H. Alfredsson. On spatial resolution issues related to time-averaged quantities. *Exp. Fluids*, 2009.

[23] S. B. Pope. *Turbuloent Flows*. Cambridge University Press, 2000.

[24] O. Reynolds. An experimental investigation of the circumstances which determine whether the motion of water shall be direct or sinnons, and of the law of resistance in parallel channels. *Proc. R. Soc.*, 1883.

[25] L. F. Richardson. *Weather Prediction by numerical Process*. Cambridge University Press, 1922.

[26] A. Segalini, A. Cimarelli, J.-D. Ruedi, E. De Angelis, and A. Talamelli. Effect of the spatial filtering and alignement error of hot-wire probes in a wall-bounded turbulent flow. *Meas. Sci. Technol.*, 2011a.

[27] A. Segalini, R. Örlü, P. Schlatter, P. H. Alfredsson, J.-D. Ruedi, and A. Talamelli. A method to estimate turbulence intensity and transverse taylor microscale in turbulent flows from spatially averaged hot-wire data. *Exp. Fluids*, 2011b.

[28] A. J. Smits, B. McKeon, and I. Marusic. High-reynolds number wall turbulence. *Annu. Rev. Fluid Mech.*, 2011a.

[29] A. J. Smits, J. Monty, M. Hultmark, S. C. Bailey, N. Hutchins, and I. Marusic. Spatial resolution correction for wall-bounded turbulence measurements. *J. Fluid. Mech*, 2011b.

[30] A. Talamelli, F. Persiani, J. H. M. Fransson, and H. Alfredsson. Ciclope, a response to the need for high reynolds number experiments. *Fluid Dyn. Res.*, 2009.

[31] C. Tropea, A. L. Yarin, and J. F. Foss. *Springer handbook of experimental fluid mechanics*. Springer, 2007.

[32] B. G. van der Hegge Zijnen. On the construction of hot-wire anemometers for the investigation of turbulence. *Appl. Sci. Res.*, 1951.

[33] P. D. Welch. The use of fast fourier transform for the estimation of power spectra: a method based on time averaging over short, modified periodograms. *IEEE T. Audio Electroacoust.*, 1967.

[34] F. White. *Viscous Fluid Flow*. Mc Graw Hill, 1991.

[35] W. W. Willmarth and S. K. Sharma. Study of turbulent structures with hot wires smaller than the viscous length. *J. Fluid. Mech*, 1984.

[36] E.-S. Zanoun, F. Durst, and J. M. Shi. The physics of heat transfer from hot wires in the proximity of walls of different materials. *Int. J. Heat Mass Tran.*, 2009.